

DTIC FILE COPY

Naval Research Laboratory

Washington, DC 20375-5000



2

NRL Memorandum Report 6333

AD-A200 349

**Beam Profile Studies for a One Eighth Betatron Wavelength
Final Focusing Cell Following Phase Mixed Transport**

J. J. WATROUS

*National Research Council
Naval Research Laboratory
Research Associate*

P. F. OTTINGER

*Plasma Technology Branch
Plasma Physics Division*

DTIC
SELECTED
NOV 16 1988
S D
D Cg

October 26, 1988

88 11 15 059

SECURITY CLASSIFICATION OF THIS PAGE

REPORT DOCUMENTATION PAGE				Form Approved OMB No 0704-0188	
1a REPORT SECURITY CLASSIFICATION UNCLASSIFIED			1b RESTRICTIVE MARKINGS		
2a SECURITY CLASSIFICATION AUTHORITY			3 DISTRIBUTION/AVAILABILITY OF REPORT Approved for public release; distribution unlimited.		
2b DECLASSIFICATION/DOWNGRADING SCHEDULE					
4 PERFORMING ORGANIZATION REPORT NUMBER(S) NRL Memorandum Report 6333			5 MONITORING ORGANIZATION REPORT NUMBER(S)		
6a NAME OF PERFORMING ORGANIZATION Naval Research Laboratory		6b OFFICE SYMBOL (if applicable) Code 4770	7a NAME OF MONITORING ORGANIZATION		
6c ADDRESS (City, State, and ZIP Code) Washington, DC 20375-5000			7b ADDRESS (City, State, and ZIP Code)		
8a NAME OF FUNDING/SPONSORING ORGANIZATION DOE		8b OFFICE SYMBOL (if applicable)	9 PROCUREMENT INSTRUMENT IDENTIFICATION NUMBER		
8c ADDRESS (City, State, and ZIP Code) Washington, DC 20545			10 SOURCE OF FUNDING NUMBERS		WORK UNIT ACCESSION NO
			PROGRAM ELEMENT NO	PROJECT NO	TASK NO DE AI 08-79 DP40092
					DN680-382
11 TITLE (Include Security Classification) Beam Profile Studies for a One Eighth Betatron Wavelength Final Focusing Cell Following Phase Mixed Transport					
12 PERSONAL AUTHOR(S) Watrous,* J. and Ottinger, P.F.					
13a TYPE OF REPORT Interim		13b TIME COVERED FROM _____ TO _____		14 DATE OF REPORT (Year, Month, Day) 1988 October 26	15 PAGE COUNT 63
16 SUPPLEMENTARY NOTATION *National Research Council/Naval Research Laboratory Research Associate Identical manuscript submitted for publication in The Physics of Fluids.					
17 COSATI CODES			18 SUBJECT TERMS (Continue on reverse if necessary and identify by block number)		
FIELD	GROUP	SUB-GROUP	Ion beams	Inertial confinement fusion	
			Transport channels	Final focusing	
19 ABSTRACT (Continue on reverse if necessary and identify by block number) The focusing properties of a one eighth betatron wavelength focusing cell are used to determine to what extent a modification of the initial phase space distribution of an ion beam can alter the number density profile of the beam at the focal plane. It is shown that the main modification is to alter the natural 1/r profile to include an off-axis peak. The relative difficulty with which the ion beams can be concentrated into this off-axis peak is then considered. Estimates of the source brightness (extraction ion diode source current density divided by the square of the microdivergence) required to deliver a given amount of beam current into a given annular region at the focal plane are derived.					
20 DISTRIBUTION/AVAILABILITY OF ABSTRACT <input checked="" type="checkbox"/> UNCLASSIFIED/UNLIMITED <input type="checkbox"/> SAME AS RPT <input type="checkbox"/> DTIC USERS			21 ABSTRACT SECURITY CLASSIFICATION UNCLASSIFIED		
22a NAME OF RESPONSIBLE INDIVIDUAL P.F. Ottinger			22b TELEPHONE (Include Area Code) (202) 767-2610		22c OFFICE SYMBOL Code 4771

DD Form 1473, JUN 86

Previous editions are obsolete

SECURITY CLASSIFICATION OF THIS PAGE

S/N 0102-LF-014-6603

BEAM PROFILE STUDIES FOR A ONE EIGHTH BETATRON WAVELENGTH FINAL FOCUSING CELL FOLLOWING PHASE MIXED TRANSPORT

I. Introduction

Light ion beam inertial confinement fusion experiments being conducted on PBFA II at Sandia National Laboratories currently employ barrel geometry applied-B ion diodes¹. In diodes of this geometry, ions are produced on the inner surface of a barrel shaped structure and are focused over a distance of less than a meter to the centerline of the barrel². The close proximity between the target and the accelerator structure could lead to significant radioactive contamination of the accelerator. One possible scheme for avoiding this problem is to use extraction geometry ion diodes to focus the ion beams into z-discharge plasma channels³. The z-discharges serve as transport channels for the ion beams. They can provide complete charge and current neutralization for the propagating beams^{4,5}, and because of the azimuthal magnetic field created by the discharge current, the beam ions can be confined to propagate within the channel radius⁶. Transport channels that are several meters in length can provide sufficient standoff between the target and the accelerator to protect the accelerator from the deleterious effects of the target explosion. In addition the length of the transport channels allows the ion beam to be spatially bunched by the use of a carefully programmed accelerator voltage waveform⁷. This bunching is crucial for producing the power level and short duration pulse needed to drive the target.

A problem with channel transport of intense ion beams is that losses associated with collisions, instabilities, and the hydrodynamic response of the channel to the passage of the beam can become very severe in small radius channels. However, these losses can be decreased by increasing the channel radius⁸. For example, for parameters of interest to the Advanced Pulse Experiment (APEX) of Sandia National Laboratories (30 MeV Li^{+3}_7 ion beams carrying MA level currents with pulse durations of 10 -

50 ns), channels with radii of 2 to 3 cm are required to sufficiently minimize the beam losses. The problem with large radius transport is it results in a mismatch between the beam radius and the target radius which is 1 cm or less.

A solution to this radius mismatch problem is to place some type of ion beam focusing cell at the exit of the transport channel. A proposed focusing cell which is currently under theoretical and experimental investigation is the one eighth betatron wavelength final focusing concept⁹. In this concept the focusing cell consists of a short, high current z-discharge. As an ion beam enters the focusing cell, the sudden increase in the azimuthal magnetic field strength over that in the transport channel causes the ion beam to pinch inward. At the exit of the focusing cell, the majority of the beam ions have negative radial velocities so that the beam comes to a focus at a short distance past the exit of the cell. The beam radius at the focal plane is determined by the ratio of the transport channel discharge current to the final focusing cell discharge current.

The natural tendency of the one eighth betatron wavelength focusing cell¹⁰ is to produce a focused ion beam number density profile that varies as $1/r$. However, the initial phase space distribution of the ion beam can be chosen so that the $1/r$ profile includes an off-axis peak. Figure 1 shows an example of a typical $1/r$ -like number density profile. This profile corresponds to a beam that was transported through a 3 cm radius, 25 kA discharge current z-discharge and focused with a 175 kA one eighth betatron wavelength focusing cell. The ion beam was injected into the channel in such a way that its initial radial phase space distribution filled a rectangular region in the radial phase space plane defined by $0 < r < 2.12$ cm and $0 < |v_r/v_b| < 0.0598$, where $v_b = (v_r^2 + v_z^2)^{1/2}$. Beam ions had no angular momentum ($v_\theta = 0$). Figure 2 shows an extreme example of

a number density profile with an off-axis peak. The difference between this example and that in Figure 1 is that ions were injected into the transport channel with initial radii and pitch angles satisfying $1.94 \text{ cm} < r < 2.12 \text{ cm}$ and $0.0548 < |v_r/v_b| < 0.0598$. In this second example, the area of radial phase space covered by the ion beam at the point of injection into the transport channel was much smaller than that in the first example (9.0×10^{-4} cm-radians compared to 1.3×10^{-1} cm-radians). Thus, to deliver the same beam current in the second example as in the first, the ion source must be much brighter. One purpose of this paper is to show how the brightness of the ion source must increase if the focused beam is to have a high concentration of ions in an off-axis peak. In the next section, the theory of one eighth betatron wavelength focusing is described qualitatively. Section III will use that theory to describe how the initial beam injection conditions must change if the focused beam is to be concentrated in an annular region. These results will be coupled to two simple models of extraction ion diodes to determine the ion source brightness requirements. These requirements will indicate the degree of difficulty involved with modifying the focused beam number density profile solely by modifying the initial ion beam phase space distribution. In Section IV, the efficiency with which an ion beam is delivered to any given annular region is calculated. Section V summarizes the results of this investigation.

II. The Theory of One Eighth Betatron Wavelength Focusing

The mathematical description of one eighth betatron wavelength focusing of intense ion beams is based on a Vlasov equation analysis of charge and current neutralized propagation of zero angular momentum ions in the z-discharge plasma of both the transport channel and the final focusing cell¹⁰. While the mathematical details of that theory will not be repeated here, the qualitative features of the theory will be presented along with the results that will be required in the next section.

Figure 3 illustrates the main components of the beam production, transport and focusing system. The ions are produced and accelerated in the extraction ion diode, which also focuses the ions onto the entrance of the transport channel. The transport channel is a long z-discharge plasma. The density of the plasma in the discharge is sufficiently high that the ion beam is completely charge and current neutralized, while it is not so high as to cause a large amount of collisional energy loss as the beam propagates. The azimuthal magnetic field associated with the discharge current confines the beam ions to travel within the discharge radius as long as they enter the channel at sufficiently small radii and with sufficiently small pitch angles. The final focusing cell is a short z-discharge with a discharge current several times higher than that in the transport channel. The sharp increase in the magnetic field strength experienced by the beam as it moves out of the transport channel and into the focusing cell causes the beam envelope to pinch inward. The length of the focusing cell is chosen so that at its exit, the beam is midway into its pinching phase. The beam will then continue to pinch inward as it propagates through field free space. This ballistic propagation distance, which is comparable to the length of the focusing cell, is considered to be important for isolating the target from the plasma in the focusing cell.

The dense plasma of the transport channel and of the final focusing cell can completely charge and current neutralize the ion beam^{4,5}. The ion beam can thus be regarded as a collection of ions propagating independently of one another under the influence of the azimuthal magnetic field produced by the discharge current. Under this condition, a single particle analysis is helpful for describing most of the essential physics of transport and focusing. A beam ion in the transport channel feels a restoring force in the radial direction due to the radial component of the $v \times B$ force. This causes the ion to execute an approximately sinusoidal trajectory called a betatron orbit as it travels down the length of the channel. The wavelength of this trajectory, i.e. the axial distance between turning points on the same side of the axis, is determined by the ion energy, charge, and mass, the channel radius, and the discharge current. In what is known as the paraxial approximation, all ions have the same betatron wavelength given by

$$\lambda_{\beta} = 2\pi r_c \sqrt{\frac{mc^2}{q} \frac{v_b}{2I_c}}, \quad (1)$$

where all quantities are measured in cgs-es units. For example, a 30 MeV Li^{+3}_7 ion in 3 cm radius channel carrying 100 kA of discharge current has a betatron wavelength of 111 cm. The paraxial approximation is valid for ions with small pitch angles; it allows the axial component of the velocity in the radial equation of motion to be replaced by the ion speed v_b , which is constant. Assuming that the magnetic field is distributed according to $B_{\theta}(r) = (2I_c/cr_c) \times (r/r_c)$, the trajectory of an ion is determined by

$$\frac{d^2 r}{dt^2} = -\frac{q}{c} \frac{2I_c}{cr_c} \frac{r}{r_c} v_z = -\frac{q}{c} \frac{2I_c}{cr_c} \frac{r}{r_c} v_b \quad (2)$$

In the paraxial approximation, this is the equation describing a simple harmonic oscillator. In the radial phase space plane, the motion of an ion traces out an ellipse defined by

$$r^2 + \left(\frac{\lambda\beta}{2\pi}\right)^2 \left(\frac{v_r}{v_b}\right)^2 = r_{tp}^2, \quad (3)$$

where r_{tp} is the turning point of the ion. Eq. (3) shows that for the turning point to be equal to or less than the channel radius, the discharge current must be sufficiently strong. The discharge current required to confine a beam ion that enters the channel at radius r_E with radial velocity v_{rE} can be found by setting the turning point in Eq. (3) equal to the channel radius and solving for I_c . This gives

$$I_c = \frac{mc^2 v_b}{2q} \frac{(v_{rE}/v_b)^2}{(1 - r_E^2/r_c^2)}. \quad (4)$$

By setting r_E and v_{rE} to the largest values that characterize the ion beam radial phase space distribution at the channel entrance this result can be interpreted as a lower bound on the discharge current required to confine the ion beam. Note that this relationship can also be obtained from the equation of conservation of canonical axial momentum without invoking the paraxial approximation. When the ion

reaches the final focusing cell, its trajectory in radial phase space changes from the ellipse given by Eq. (3) to a different ellipse defined by an equation of the same form as Eq. (3), but with the final focusing cell discharge current used to determine the betatron wavelength. This new ellipse is narrower in radial extent and broader in the radial velocity direction.

The behavior of a beam propagating in the transport channel is determined by the collective behavior of the individual beam ions. In the paraxial approximation, each ion travels on an ellipse in the radial phase space plane, and the axial distance required to complete an elliptical orbit, i.e. the betatron wavelength, is the same for all ions. Thus, whatever initial radial phase space distribution of ions is injected into the channel, it reappears at intervals of the betatron wavelength. Between these reappearances the radial phase space distribution rotates on a fixed ellipse in the radial phase space plane. If the paraxial approximation is not made, then the betatron wavelength of an ion depends on its turning point. Thus, if the initial radial phase space distribution is such that there is a spread in turning points, and this is the case for all but a highly contrived distribution, there will then be a corresponding spread in the betatron wavelengths. Because of this spread the ion beam radial phase space distribution will be a quasiperiodic function of the propagation distance, rather than being a simple periodic function as in the paraxial approximation. The initial distribution will still reappear at intervals of the betatron wavelength, but at each reappearance, it will be slightly more deformed than it was at the previous appearance. After many betatron wavelengths of propagation, this gradual deformation causes the ion beam radial phase space distribution to effectively fill in the elliptical region in the radial phase space plane defined by the smallest and the largest turning points in the ion beam distribution. For example, the rectangular initial phase space distribution defined by $r_1 \leq r \leq r_2$, $v_{r1} \leq |v_r| \leq v_{r2}$ shown in Figure 4 fills in the area between the

ellipses (denoted by the dashed curves) defined by

$$r_1^2 + \left(\frac{\lambda_\beta}{2\pi}\right)^2 \left(\frac{v_{r1}}{v_b}\right)^2 \leq r^2 + \left(\frac{\lambda_\beta}{2\pi}\right)^2 \left(\frac{v_r}{v_b}\right)^2 \leq r_2^2 + \left(\frac{\lambda_\beta}{2\pi}\right)^2 \left(\frac{v_{r2}}{v_b}\right)^2 \quad (5)$$

after many betatron wavelengths of propagation. Phase mixing makes the ion beam radial phase space distribution independent of the propagation distance. It is assumed in this analysis that the ion beam is completely phase mixed by the time it reaches the final focusing cell.

When the ion beam enters the final focusing cell, the phase space ellipses defined by Eq. (5) undergo a deformation in response to the abrupt change in the magnetic field strength. If the magnetic field has the same distribution in the final focusing cell as that which has been assumed for the transport channel, i.e. $B_\theta(r) = (2I_f/cr_c) \times (r/r_c)$, where I_f is the final focusing cell discharge current, then this deformation is a rigid clockwise rotation. It is convenient in describing this deformation to use a slightly different phase space plane. Let $\Gamma = (\lambda_\beta/2\pi)(v_r/v_b)$, where λ_β is the betatron wavelength of a beam ion in the final focusing cell (Eq. (1) using I_f in place of I_c). The phase space trajectory of an ion passing through the focusing cell is a circle, rather than an ellipse, in this new r - Γ phase space plane. In the r - Γ plane the elliptical annulus occupied by the beam undergoes a rigid clockwise rotation such that the angle that its major axis makes with respect to the r -axis is $-2\pi z/\lambda_\beta$ radians. Thus, after a distance of one eighth of a betatron wavelength, the ellipses have rotated -45° . At this point, the number of ions with negative radial velocities is maximized. The beam then

enters field free space and propagates ballistically to the target. While it does so, the ellipses in the r - Γ plane continue to rotate and undergo an area preserving deformation marked by a progressive increase in the eccentricity. At the focal plane, the ellipses have rotated a total of -90° from where they started at the entrance to the final focusing cell, and the ion beam occupies the area in radial phase space defined by

$$\left(\frac{2}{2+\Delta}\right) \left[r_1^2 + \left(\frac{\lambda\beta}{2\pi}\right)^2 \left(\frac{v_{r1}}{v_b}\right)^2 \right] \leq r^2 + \left(\frac{\lambda\beta}{2\pi}\right)^2 \left(\frac{v_r}{v_b}\right)^2 \quad (6)$$

$$\leq \left(\frac{2}{2+\Delta}\right) \left[r_2^2 + \left(\frac{\lambda\beta}{2\pi}\right)^2 \left(\frac{v_{r2}}{v_b}\right)^2 \right],$$

where $\Delta = I_f/I_c - 1$. In the usual case, r_2 , v_{r2} , and the channel discharge current are chosen so that the maximum turning point is equal to the channel radius. This makes the fullest use of the available magnetic field strength. Thus, the beam is focused to a spotsize of $[2/(2+\Delta)]^{1/2} r_c$.

To this point, the theory is independent of the exact form of the initial radial phase space distribution. After transport, the beam is confined to an elliptical annulus in the radial phase space plane with the inner and outer radii of this annular region corresponding to the smallest and the largest turning points, respectively, that will occur in that distribution. This is illustrated in Fig. 4. However, to calculate number density profiles, the exact form of the initial radial phase space distribution must be specified. For the purposes of this calculation, the initial radial phase space distributions that have been considered are the family of rectangles defined by

$r_1 < r < r_2$, $|v_{r1}| < |v_r| < |v_{r2}|$. Within this rectangular region of radial phase space, ions are distributed in such a manner as to produce a number density profile that is flat between r_1 and r_2 . Because of the cylindrical geometry, this means that the initial radial phase space distribution is more heavily weighted at larger radii. This initial distribution is convenient for calculations and is also a useful model for the possible distributions produced by an extraction ion diode. After phase mixing, the phase space distribution of the beam depends only on the distance from the origin of the phase space plane, apart from a $1/r$ factor that reflects the cylindrical geometry. At the focal plane, the distribution can be expressed as a function of ρ , where ρ is defined by

$$\rho^2 = \frac{(2 + \Delta)}{2} r^2 + \frac{2(1 + \Delta)}{(2 + \Delta)} r_1^2 \quad (7)$$

It is also convenient to express the combination $(\lambda_p/2\pi)v_r/v_b$ as a new variable γ . In the r - γ phase space plane, analogous to the r - Γ phase space used for describing the focusing cell, the phase space trajectory of an ion in the transport channel is a circle rather than an ellipse. There are then two results, depending on the magnitude of $(\gamma_2^2 + r_1^2)^{1/2}$ relative to $(r_2^2 + \gamma_1^2)^{1/2}$. The two results correspond to the orientation of the rectangle that defines the initial radial phase space distribution. For $\gamma_2^2 + r_1^2 < r_2^2 + \gamma_1^2$, that rectangle is oriented horizontally, and the focused beam phase space distribution is

$$f^{pm} = \frac{2N}{\pi r} \delta(v_\theta) \frac{\delta(v - v_b)}{v} \left\{ \begin{array}{ll} 0; & \rho^2 < r_1^2 + \gamma_1^2 \\ \sqrt{\rho^2 - r_1^2} - \gamma_1; & r_1^2 + \gamma_1^2 < \rho^2 \\ \gamma_2 - \gamma_1; & \rho^2 < r_1^2 + \gamma_2^2 \\ \gamma_2 - \sqrt{\rho^2 - r_1^2}; & r_1^2 + \gamma_2^2 < \rho^2 \\ 0; & \rho^2 < r_2^2 + \gamma_1^2 \\ & r_1^2 + \gamma_1^2 < \rho^2 \\ & \rho^2 < r_2^2 + \gamma_1^2 \\ & r_2^2 + \gamma_1^2 < \rho^2 \\ & \rho^2 < r_2^2 + \gamma_2^2 \\ & \rho^2 > r_2^2 + \gamma_2^2 \end{array} \right. \quad (8)$$

For $\gamma_2^2 + r_1^2 > r_2^2 + \gamma_1^2$, the initial phase space distribution rectangle is oriented vertically, and the focused beam phase space distribution is

$$f^{pm} = \frac{2N}{\pi r} \delta(v_\theta) \frac{\delta(v - v_b)}{v}$$

0;	$\rho^2 < r_1^2 + \gamma_1^2$
$\sqrt{\rho^2 - r_1^2} - \gamma_1$;	$r_1^2 + \gamma_1^2 < \rho^2$ $\rho^2 < r_2^2 + \gamma_1^2$
$\sqrt{\rho^2 - r_1^2} - \sqrt{\rho^2 - r_2^2}$;	$r_2^2 + \gamma_1^2 < \rho^2$ $\rho^2 < r_2^2 + r_1^2$ (9)
$\gamma_2 - \sqrt{\rho^2 - r_1^2}$;	$\gamma_2^2 + r_1^2 < \rho^2$ $\rho^2 < r_2^2 + \gamma_2^2$
0;	$\rho^2 > r_2^2 + \gamma_2^2$

where in both Eqs. (8) and (9), N represents the average density of ions in the region of the radial phase space plane occupied by the initial phase space distribution. For both equations, if N_0 is the total number of ions present at the source plane, then N is given by $N = N_0 \lambda_\beta / 2\pi(r_2^2 - r_1^2)(\gamma_2 - \gamma_1)$. The number density profile of the beam at the focal plane is then obtained by integrating either Eq. (8) or (9) over the radial velocity. The complete expressions for the number density profile at the focal plane are given in the Appendix. These results can be used to show that any off-axis peak in the focused beam number density profile occurs between radii that correspond to the intersection of the ellipse defined by the phase mixed radial phase space distribution and the v_r axis, i.e. the range of radii given by Eq. (6) with $v_r = 0$.

III. Estimates of Required Source Brightness

As discussed in the previous Section, the number density profile of the focused ion beam depends on the initial radial phase space distribution. For the model initial distribution chosen for this analysis, in which the ions occupy a rectangular region in the radial phase space plane, the focused beam density profile depends only on the relative positions of the four corners of that rectangular region. In order to produce a focused ion beam number density profile that has a strong off-axis peak, the initial distribution must be strongly concentrated in a small region of the radial phase space plane away from $r = 0$. The "narrower" the initial distribution is, the stronger will be the off-axis peak, where "narrow" refers to the span of distances from the origin of the radial phase space plane. For the rectangular initial distribution used here, the relevant dimension is the length of the diagonal. To deliver the same ion beam current with a narrower initial distribution requires that the ion source concentrate an equal number of ions into a smaller area in the radial phase space plane, i.e. the source brightness must increase as the area of the radial phase space plane spanned by the initial distribution decreases. To estimate the required source brightness, it will be required that the elliptical annulus that defines the phase mixed and focused ion beam radial phase space distribution intersect the v_r axis in a range of radii that corresponds to a target annulus defined by $r_{in} \leq r \leq r_{out}$, as illustrated in Figure 5. By using the transport and focusing theory discussed in the previous Section, this requirement can be translated into a calculation of the source brightness. This requirement is a minimum condition for concentrating the beam onto a target annulus but does not account for the ions which miss the target annulus at the focal plane. In the next Section, these ions will be accounted for through the calculation of a delivery efficiency.

As mentioned previously, the off-axis peak in the focused beam number density profile occurs within the range of radii given by Eq. (6) with

$v_r = 0$. The outer radius of this range can be chosen by using the appropriate ratio of discharge currents. The inner radius of this range is determined by r_1 and v_{r1} . It will be assumed that r_2 and v_{r2} are chosen such that

$$r_2^2 + \left(\frac{\lambda\beta}{2\pi}\right)^2 \left(\frac{v_{r2}}{v_b}\right)^2 = r_c^2. \quad (10)$$

The required ratio of the transport channel discharge current to the final focusing cell discharge current is then determined by

$$r_{out} = \sqrt{\frac{2}{2+\Delta}} r_c, \quad (11)$$

$$\text{i.e.} \quad \frac{I_f}{I_c} = 2 \left(\frac{r_c}{r_{out}}\right)^2 - 1. \quad (12)$$

From Eq. (6), and using Eq. (11) to eliminate the factor $2/(2+\Delta)$, r_1 and v_{r1} must satisfy

$$r_1^2 + \left(\frac{\lambda_g}{2\pi}\right)^2 \left(\frac{v_{r1}}{v_b}\right)^2 = \left(\frac{r_{in}}{r_{out}}\right)^2 r_c^2. \quad (13)$$

Eq. (13) then determines the injection conditions in terms of the location of the off-axis peak in the number density profile of the focused ion beam.

To obtain requirements on the ion beam source, specific injection schemes must be considered. Two such schemes will be considered here. One scheme, illustrated by Figure 6, corresponds to the conventional extraction diode focusing scheme. The extraction diode is designed to focus to a point; the spot size is limited by microdivergence. This scheme will be called pinched focusing. The second scheme is illustrated in Figure 7. In this scheme the extraction diode is designed to produce a beam that is hollow at the entrance to the transport channel, with the width of the annulus determined by microdivergence. This scheme will be called annular focusing. Rather than dealing explicitly with the radial velocities, the pitch angles α_1 and α_2 will be used where $\alpha_1 = v_{r1}/v_b$ and $\alpha_2 = v_{r2}/v_b$. For both focusing schemes it will be assumed that the pitch angles at injection are determined primarily by the injection geometry. This assumption is valid as long as the microdivergence is sufficiently small. The anode of the extraction diode will be modeled as an annulus with outer radius R_{out} and inner radius R_{in} . The focal length of the diode will be denoted by F . The maximum and minimum pitch angles at injection can then be expressed as

$$\alpha_1 = R_{out}/F \quad \text{and} \quad \alpha_2 = R_{in}/F \quad (14)$$

These considerations allow the source current density required to produce a given ion beam current to be calculated as a function of the diode focal length and microdivergence. This will be done first for the pinched focus, then for the annular focus.

Pinched Focus

In this injection scheme, $r_1 = 0$ and r_2 is determined by microdivergence:

$$r_2 = F \Delta\theta \quad (15)$$

The anode surface is modeled as an annulus; the inner and outer radii determine both the area available for production of the ion beam and the minimum and maximum injection angles. The anode must produce the required ion beam current. This requires a certain anode current density J_A given by

$$J_A = \frac{I_B}{\pi(R_{out}^2 - R_{in}^2)}, \quad (16)$$

where I_B is the ion beam current in the diode. Of course, in reality the anode current density would have some spatial structure, both in radius and in azimuth, but its average over the anode area must equal that given by Eq. (16).

The maximum injection angle is determined by the requirement that ions are confined to the transport channel. From Eqs. (10) and (15), the maximum angle can be calculated as

$$\alpha_2 = \frac{2\pi}{\lambda_\beta} \left[r_c^2 - F^2(\Delta\theta)^2 \right]^{1/2}. \quad (17)$$

The minimum injection angle is determined by Eq. (13) with $r_1 = 0$. This gives

$$\alpha_1 = \frac{2\pi}{\lambda_\beta} \frac{r_{in}}{r_{out}} r_c \quad (18)$$

Using the relation between the anode radii and the injection angles given in Eq. (14) yields the equation for the anode current density

$$J_A = \frac{I_B}{\pi} \left(\frac{\lambda_B}{2\pi} \right)^2 \frac{1}{F^2} \frac{1}{(1-f^2)r_c^2 - F^2(\Delta\theta)^2}, \quad (19)$$

where $f = r_{in}/r_{out}$. The anode current density can be minimized with respect to the focal length F yielding the optimal focal length

$$F_{opt} = \frac{\sqrt{1-f^2}}{\sqrt{2} \Delta\theta} r_c. \quad (20)$$

At the optimal focal length, the anode current density attains a minimum given by

$$J_{A,min} = \frac{I_B}{\pi r_c^4} \left(\frac{\lambda_B}{2\pi} \right)^2 \frac{4(\Delta\theta)^2}{(1-f^2)^2}. \quad (21)$$

These results are plotted in Figs. 8, 9, and 10. In these figures, and in all of the figures to follow, $I_B = 3.33$ MA (30 MeV ${}^3_7\text{Li}$), $r_c = 3$ cm, and $r_{out} = 0.8$ cm. Two different values of the final focusing current are considered, 1 MA and 300 kA. For the high current case, Eq. (12) requires that $I_c = 36.9$ kA. For the low current case $I_c = 11.1$ kA. In Fig. 8, the anode current density is plotted as a function of the focal length for several different values of the microdivergence. In this plot, the final focusing current was 1 MA and $r_{in} = 6$ mm. In Figures 9 and 10, the minimum anode current density is plotted as a function of microdivergence for several different values of r_{in} for the high current case and the low current case, respectively.

Figures 11 and 12 show how the inner and outer anode radii must vary with microdivergence to achieve the minimum current density of Eq. (21). Figure 11 corresponds to the high current case, and Figure 12 to the low current case. Also shown in these plots is the optimal focal length. The anode radii were calculated from the relations $R_{in} = F\alpha_{min}$, $R_{out} = F\alpha_{max}$ using the optimal focal length.

The minimum current density of Eq. (21) depends on the microdivergence quadratically, so by dividing $J_{A,min}$ by $(\Delta\theta)^2$, a quantity that depends only on the transport, focusing, and target parameters results. Figure 13 shows a plot of this quantity as a function of r_{in} for the high current and low current cases. Multiplying this quantity by the ion energy will give the power brightness required by the target. Figure 13 shows that as the beam profile becomes progressively more annular, the required power brightness increases rapidly, spanning nearly an order of magnitude as r_{in} increases from 0 to 6 mm, then increases more rapidly as r_{in} continues to approach r_{out} .

Annular Focus

Figure 7 illustrates the annular focus injection scheme. In this scheme, $\alpha_1 = 0$. The diode microdivergence determines the spot size at the transport channel entrance through $r_2 -$

$r_1 = F\Delta\theta$. The maximum injection angle is determined by the requirement that ions be confined to the channel. The minimum injection radius is determined from Eq. (13) with $v_{r1} = 0$. Denoting this result as $r_1 = fr_c$, the maximum injection angle is given by

$$\alpha_2 = \left(\frac{2\pi}{\lambda_B}\right) \left[r_c^2 - (f r_c + F \Delta\theta)^2 \right]^{1/2}, \quad (22)$$

where, as before, $f = r_{in}/r_{out}$.

The anode surface is modeled in this scheme as a disc with radius R_{out} which is related to α_2 as indicated in Eq. (14). The required anode current density can then be written as

$$J_A = \frac{I_B}{\pi} \left(\frac{\lambda_B}{2\pi}\right)^2 \frac{1}{F^2} \frac{1}{\left[r_c^2 - (f r_c + F \Delta\theta)^2 \right]} \quad (22)$$

As in the previous case, this may be minimized with respect to the focal length F . The optimal focal length is

$$F_{opt} = \frac{r_c}{\Delta\theta} \left[-\frac{3}{4} f + \frac{1}{\sqrt{2}} \sqrt{1 + \frac{1}{8} f^2} \right] \quad (24)$$

At this optimal focal length, the required anode current density is

$$J_{A,min} = \frac{I_B}{\pi r_c^4} \left(\frac{\lambda_B}{2\pi}\right)^2 \frac{(\Delta\theta)^2}{\left[-\frac{3}{4} f + \frac{1}{\sqrt{2}} \sqrt{1 + \frac{1}{8} f^2} \right]^2 \left[1 - \left(\frac{1}{4} f + \frac{1}{\sqrt{2}} \sqrt{1 + \frac{1}{8} f^2} \right)^2 \right]} \quad (25)$$

Figures 14 and 15 show $J_{A,min}$ as a function of microdivergence for several

different values of r_{in} for the high current and low current cases, respectively. Figures 16 and 17 show the anode radius required to produce the given ion beam current with the minimum anode current density. Also plotted are the optimal focal lengths.

The minimum anode current density is, as in the previous case, quadratic in the microdivergence. Figure 18 shows how $J_{A,min}/(\Delta\theta)^2$ varies with r_{in} for both the high and low current cases. Comparing this with the similar result for the pinched focus shows that the annular focus places much more stringent requirements on the extraction diode. For the annular focusing scheme, the required power brightness increases by nearly two orders of magnitudes as r_{in} ranges from 0 to 6 mm.

IV. Calculation of Delivery Efficiency

The calculations presented in Section III were based on the requirement that the beam be injected into the channel in such a way that an off-axis peak in the focused beam number density profile occur between two given radii r_{in} and r_{out} . From Figure 2, one can see that by choosing r_1 and v_{r1} close enough to r_2 and v_{r2} , a highly peaked number density profile can be produced. However, not all of the available ions are concentrated into any given annulus at the focal plane. Thus, while the conditions on the source brightness found in the preceding Section are useful for determining how difficult it is to concentrate the beam into an off-axis peak, they are under-estimates because only a fraction of the beam is delivered to the region $r_{in} < r < r_{out}$ as illustrated in Figure 5. If one requires that a certain ion beam current be delivered to the annular region, then the estimates given in the preceding Section must be increased to account for the fraction of the ion beam that does not appear in the annular region. In this Section, the efficiency with which an ion beam is delivered to the annular region $r_{in} < r < r_{out}$ is calculated, and these results are applied to the estimates of the required source brightness from Section III.

The delivery efficiency η will be defined as the number of beam ions delivered to the annular region divided by the total number of beam ions delivered to the focal plane. Thus, η is just the ratio of the integrals of the number density

$$\eta = \frac{\int_{r_{in}}^{r_{out}} n_b(r) r dr}{\int_0^{r_{foc}} n_b(r) r dr} \quad (26)$$

where $n_b(r)$ is the number density of the ion beam at the focal plane. In the integral in the denominator of Eq. (26) r_{foc} is the radius of the focused ion beam. It has been left arbitrary to account for the possibility that the ion beam is either under or over focused with respect to r_{out} . Due to the functional form of $n_b(r)$, the integrals appearing in Eq. (26) must be calculated numerically.

An upper bound on the delivery efficiency can be obtained by considering the zero emittance limit. Suppose that all of the beam ions are injected with the largest radius and pitch angle consistent with the requirement that the ions be confined to propagate within the channel radius. The phase mixed radial phase space distribution of such a beam is given by

$$f(r, v_r) = \delta(r^2 + (\lambda_B/2\pi)^2 (v_r/v_b)^2 - r_c^2) \quad (27)$$

i.e. in the transport channel, ions are restricted to move on the circle $r^2 + \gamma^2 = r_{\text{ch}}^2$ in the r - γ plane. At the focal plane, this distribution is modified to

$$f(r, v_r) = \delta(r^2 + (\lambda_B/2\pi)^2 (v_r/v_b)^2 - \left(\frac{2}{2+\Delta}\right)r_c^2) \quad (28)$$

i.e. in the r - γ plane, ions occupy the circle of radius $[2/(2+\Delta)]r_c$. The distribution of ions on this circle is independent of the angle. Thus, the number of ions that appear in any given annular region $r_{\text{in}} < r < r_{\text{out}}$ is determined by the fraction of the circle $r^2 + \gamma^2 = [2/(2+\Delta)]r_{\text{ch}}^2$ that passes through the annulus as illustrated in Figure 19. Using r_{foc} as shorthand for $[2/(2+\Delta)]r_c$, the delivery

efficiency for the zero emittance limit is

$$\eta_{ZEL} = \frac{2}{\pi} \left[\cos^{-1} \left(\frac{r_{in}}{r_{foc}} \right) - \cos^{-1} \left(\frac{r_{out}}{r_{foc}} \right) \right] \quad (29)$$

For the case of $r_{foc} = r_{out}$ considered in the previous Section, the zero emittance limit delivery efficiency is simply

$$\eta_{ZEL} = \frac{2}{\pi} \cos^{-1} \left(\frac{r_{in}}{r_{out}} \right) \quad (30)$$

For example, the zero emittance limit delivery efficiency for $r_{in} = 0.6$ cm and $r_{out} = 0.8$ cm is 46%. The zero emittance limit delivery efficiency will be used to compare with the delivery efficiency for the more realistic cases of pinched and annular focusing.

The delivery efficiency has been calculated numerically for both the pinched focus and annular focus cases analyzed in Section III. As in Section III the injection of the beam into the transport channel was assumed to take place at the optimal focal lengths as defined by Eq. (20) for the pinched focus case and by Eq. (24) for the annular focus case. Figure 20 shows the delivery efficiency for the pinched focus case as a function of r_{in} . Also plotted in Fig. 20 is the zero emittance limit delivery efficiency. This result shows that for small values of r_{in} the efficiency is close to the zero emittance limit, but as r_{in} approaches r_{out} , it drops rapidly below η_{ZEL} . Figure 21 shows the delivery efficiency for the annular focus case. The delivery efficiency for the annular focus case is quite similar to that for the pinched focus case.

These results can be used along with the calculation of the required source brightness from Section III to determine the source brightness required to deliver a specified amount of beam current to the region $r_{in} < r < r_{out}$. This is done by dividing the source brightness plotted in either Fig. 13 or Fig. 18 by the delivery efficiency for the appropriate case. Figures 22 and 23 show the results of this calculation for the pinched focus case and for the annular focus case, respectively. In these calculations it was required that 3.33 MA of 30 MeV Li_7^{+3} ions produced at the diode (before time-of-flight bunching) be delivered to the specified annulus; the total beam current is greater than this amount by the reciprocal of the delivery efficiency. These results indicate that the requirement that the specified beam current be delivered to a given annulus places very stringent requirements on the ion source, particularly for narrow annuli. As shown in Figs. 22 and 23, the required source brightness increases, for example, by about two orders of magnitude as r_{in} increases from 4 mm to 7 mm for a target annulus with an outer radius of 8 mm.

V. Conclusions

The effect of the initial radial phase space distribution of an ion beam on its radial number density profile after being transported and focused with a one eighth betatron wavelength focusing cell has been investigated. The theory of one eighth betatron wavelength focusing of zero angular momentum ions was used to develop estimates of the source brightness required to inject an ion beam with a given current into the transport channel in such a way that at the focal plane, a number density profile with an off-axis peak located in a specified annulus would result. These estimates indicate that for reasonable values of microdivergence, the anode current density that is required to deliver the desired amount of ion beam current to the target annulus is quite high e.g. $\sim 500 \text{ kA/cm}^2$ for 15 mrad and a beam concentrated in the annulus $6 \text{ mm} < r < 8 \text{ mm}$. This is for the case of an ion beam transported through a 3 cm radius, 11.1 kA transport channel and focused with a 300 kA one eighth betatron wavelength focusing cell. However, for beams concentrated in broader annuli, the required current density is substantially lower e.g. $\sim 15 \text{ kA/cm}^2$ at 15 mrad for $r_{in} = 2 \text{ mm}$ and $r_{out} = 8 \text{ mm}$.

The effect of angular momentum has also been considered, although that analysis has not been included here. One might expect that because angular momentum causes ions to stay away from the axis, it could be helpful in producing the type of annular focus considered here. The detailed analysis of angular momentum shows that angular momentum yields no positive benefit, and in fact, tends to make an annular focus more difficult to achieve. The reason for the lack of a positive benefit may be understood intuitively by considering the effect that nonzero angular momentum has on the trajectory that an ion takes in the radial phase space plane. Figure 24 shows how the radial phase space trajectory of an ion is altered when the ion is given angular momentum. Recall that in the zero angular momentum case, the

phase space trajectory was approximately an ellipse, but, as shown in Fig. 24, angular momentum alters this trajectory by giving the ion a distance of minimum approach to the axis. The phase space trajectory of the ion is altered appreciably from its zero angular momentum trajectory only in the region near the axis. This statement holds true as the ion passes through the focusing cell and through the ballistic propagation region. Thus, the addition of angular momentum affects the focused ion beam distribution only in the region very close to the axis. This leads to the observation that angular momentum does not have an appreciable effect on enough of the ion beam phase space distribution to significantly effect that part of the distribution that is focused onto the annular target region. The only possible way in which angular momentum could have a significant effect would be if all or nearly all of the transverse energy $m(v_r^2 + v_\theta^2)/2$ available from the ion diode were invested into angular momentum, and this would require a diode that would produce little or no radial velocity. As such a diode could not rely on geometric focusing, it would have to have a very high source brightness to deliver a beam of the required current level to the transport channel. Thus, the inclusion of angular momentum is not helpful for producing the annular focused ion beam distribution considered here.

Acknowledgements

This work was supported by the U.S. Department of Energy through Sandia National Laboratories. One of the authors (JW) was a National Research Council Associate at the Naval Research Laboratory during the time this work was being performed.

Appendix

The beam number density as a function of radius is obtained by integrating the expressions for the beam phase space density, Eqs. (8) or (9), over the velocity space coordinates. For the most part, this amounts to doing integrals of the form

$$\int \sqrt{x^2 \pm a^2} dx = \frac{1}{2} \left[x \sqrt{x^2 \pm a^2} \pm a^2 \log \left(x + \sqrt{x^2 \pm a^2} \right) \right]. \quad (A1)$$

For the case of $r_2^2 + r_1^2 < r_1^2 + r_2^2$, corresponding to the phase space distribution given by Eq. (8), the number density profile is:

$$(i) \text{ for } 0 \leq r \leq \left[\frac{2}{2 + \Delta} (r_1^2 + r_2^2) \right] \quad (A2)$$

$$n_b(r) = \frac{4Nv_b}{\lambda_B r} \sqrt{\frac{1}{2} \left(\frac{2 + \Delta}{2 + \Delta} \right)} \times$$

$$\left\{ \frac{r_2}{2} \left[\sqrt{r_2^2 + r_2^2 - \left(\frac{2 + \Delta}{2} \right) r^2} - \sqrt{r_1^2 + r_2^2 - \left(\frac{2 + \Delta}{2} \right) r^2} \right] \right.$$

$$- \frac{r_1}{2} \left[\sqrt{r_2^2 + r_1^2 - \left(\frac{2 + \Delta}{2} \right) r^2} - \sqrt{r_1^2 + r_1^2 - \left(\frac{2 + \Delta}{2} \right) r^2} \right]$$

$$- \frac{1}{2} \left[r_1^2 - \left(\frac{2 + \Delta}{2} \right) r^2 \right] \log \left[\frac{r_2 + \sqrt{r_1^2 + r_2^2 - \left(\frac{2 + \Delta}{2} \right) r^2}}{r_1 + \sqrt{r_2^2 + r_1^2 - \left(\frac{2 + \Delta}{2} \right) r^2}} \right]$$

$$\left. + \frac{1}{2} \left[r_2^2 - \left(\frac{2 + \Delta}{2} \right) r^2 \right] \log \left[\frac{r_2 + \sqrt{r_2^2 + r_2^2 - \left(\frac{2 + \Delta}{2} \right) r^2}}{r_1 + \sqrt{r_2^2 + r_1^2 - \left(\frac{2 + \Delta}{2} \right) r^2}} \right] \right\}$$

$$(ii) \text{ for } \left[\frac{2}{2+\Delta}(r_1^2 + r_2^2) \right] \leq r \leq \left[\frac{2}{2+\Delta}(r_1^2 + r_2^2) \right] \quad (A3)$$

$$n_b(r) = \frac{4Nv_b}{\lambda_\beta r} \sqrt{\frac{1}{2} \left(\frac{2+\Delta}{2+\Delta} \right)} \times$$

$$\left\{ \frac{r_2}{2} \left[\sqrt{r_2^2 + r_2^2 - \left(\frac{2+\Delta}{2} \right) r^2} - \sqrt{r_1^2 + r_2^2 - \left(\frac{2+\Delta}{2} \right) r^2} \right] \right.$$

$$\left. - \frac{r_1}{2} \left[\sqrt{r_2^2 + r_1^2 - \left(\frac{2+\Delta}{2} \right) r^2} \right] \right.$$

$$\left. - \frac{1}{2} \left[r_1^2 - \left(\frac{2+\Delta}{2} \right) r^2 \right] \log \left[\frac{r_2 + \sqrt{r_1^2 + r_2^2 - \left(\frac{2+\Delta}{2} \right) r^2}}{\sqrt{\left(\frac{2+\Delta}{2} \right) r^2 - r_1^2}} \right] \right.$$

$$\left. + \frac{1}{2} \left[r_2^2 - \left(\frac{2+\Delta}{2} \right) r^2 \right] \log \left[\frac{r_2 + \sqrt{r_2^2 + r_2^2 - \left(\frac{2+\Delta}{2} \right) r^2}}{r_1 + \sqrt{r_2^2 + r_1^2 - \left(\frac{2+\Delta}{2} \right) r^2}} \right] \right\}$$

$$\text{(iii) for } \left[\frac{2}{2+\Delta}(r_1^2 + r_2^2) \right] \leq r \leq \left[\frac{2}{2+\Delta}(r_2^2 + r_1^2) \right] \quad (\text{A4})$$

$$n_b(r) = \frac{4Nv_b}{\lambda_B r} \sqrt{\frac{1}{2} \left(\frac{2+\Delta}{2+\Delta} \right)} \times$$

$$\left\{ \frac{r_2}{2} \sqrt{r_2^2 + r_2^2 - \left(\frac{2+\Delta}{2} \right) r^2} - \frac{r_1}{2} \sqrt{r_2^2 + r_1^2 - \left(\frac{2+\Delta}{2} \right) r^2} \right.$$

$$\left. + \frac{1}{2} \left[r_2^2 - \left(\frac{2+\Delta}{2} \right) r^2 \right] \log \left[\frac{r_2 + \sqrt{r_2^2 + r_2^2 - \left(\frac{2+\Delta}{2} \right) r^2}}{r_1 + \sqrt{r_2^2 + r_1^2 - \left(\frac{2+\Delta}{2} \right) r^2}} \right] \right\}$$

$$\text{(iv) for } \left[\frac{2}{2+\Delta}(r_2^2 + r_1^2) \right] \leq r \leq \left[\frac{2}{2+\Delta}(r_2^2 + r_2^2) \right] \quad (\text{A5})$$

$$n_b(r) = \frac{4Nv_b}{\lambda_B r} \sqrt{\frac{1}{2} \left(\frac{2+\Delta}{2+\Delta} \right)} \times$$

$$\left\{ \frac{r_2}{2} \sqrt{r_2^2 + r_2^2 - \left(\frac{2+\Delta}{2} \right) r^2} \right.$$

$$\left. + \frac{1}{2} \left[r_2^2 - \left(\frac{2+\Delta}{2} \right) r^2 \right] \log \left[\frac{r_2 + \sqrt{r_2^2 + r_2^2 - \left(\frac{2+\Delta}{2} \right) r^2}}{\sqrt{\left(\frac{2+\Delta}{2} \right) r^2 - r_2^2}} \right] \right\}$$

For the case of $\gamma_2^2 + r_1^2 \geq \gamma_1^2 + r_2^2$, corresponding to the phase space density given by Eq. (9), the number density profile is

$$(i) \text{ for } 0 \leq r \leq \left[\frac{2}{2 + \Delta} (r_1^2 + \gamma_1^2) \right] \quad (A6)$$

$$n_b(r) = \frac{4Nv_b}{\Lambda \beta r} \sqrt{\frac{1}{2} \left(\frac{2 + \Delta}{2 + \Delta} \right)} \times$$

$$\left\{ \frac{\gamma_2}{2} \left[\sqrt{r_2^2 + \gamma_2^2 - \left(\frac{2 + \Delta}{2} \right) r^2} - \sqrt{r_1^2 + \gamma_2^2 - \left(\frac{2 + \Delta}{2} \right) r^2} \right] \right.$$

$$- \frac{\gamma_1}{2} \left[\sqrt{r_2^2 + \gamma_1^2 - \left(\frac{2 + \Delta}{2} \right) r^2} - \sqrt{r_1^2 + \gamma_1^2 - \left(\frac{2 + \Delta}{2} \right) r^2} \right]$$

$$- \frac{1}{2} \left[r_1^2 - \left(\frac{2 + \Delta}{2} \right) r^2 \right] \log \left[\frac{\gamma_2 + \sqrt{r_1^2 + \gamma_2^2 - \left(\frac{2 + \Delta}{2} \right) r^2}}{\gamma_1 + \sqrt{r_2^2 + \gamma_1^2 - \left(\frac{2 + \Delta}{2} \right) r^2}} \right]$$

$$\left. + \frac{1}{2} \left[r_2^2 - \left(\frac{2 + \Delta}{2} \right) r^2 \right] \log \left[\frac{\gamma_2 + \sqrt{r_2^2 + \gamma_2^2 - \left(\frac{2 + \Delta}{2} \right) r^2}}{\gamma_1 + \sqrt{r_2^2 + \gamma_1^2 - \left(\frac{2 + \Delta}{2} \right) r^2}} \right] \right\}$$

$$(ii) \text{ for } \left[\frac{2}{2+\Delta}(r_1^2 + \gamma_1^2) \right] \leq r \leq \left[\frac{2}{2+\Delta}(r_2^2 + \gamma_1^2) \right] \quad (A7)$$

$$n_b(r) = \frac{4Nv_b}{\Lambda_\beta r} \sqrt{\frac{1}{2} \left(\frac{2+\Delta}{2+\Delta} \right)} \times$$

$$\left\{ \frac{\gamma_2}{2} \left[\sqrt{r_2^2 + \gamma_2^2 - \left(\frac{2+\Delta}{2} \right) r^2} - \sqrt{r_1^2 + \gamma_2^2 - \left(\frac{2+\Delta}{2} \right) r^2} \right] \right.$$

$$- \frac{\gamma_1}{2} \left[\sqrt{r_2^2 + \gamma_1^2 - \left(\frac{2+\Delta}{2} \right) r^2} \right]$$

$$- \frac{1}{2} \left[r_1^2 - \left(\frac{2+\Delta}{2} \right) r^2 \right] \log \left[\frac{\gamma_2 + \sqrt{r_1^2 + \gamma_2^2 - \left(\frac{2+\Delta}{2} \right) r^2}}{\sqrt{\left(\frac{2+\Delta}{2} \right) r^2 - r_1^2}} \right]$$

$$\left. + \frac{1}{2} \left[r_2^2 - \left(\frac{2+\Delta}{2} \right) r^2 \right] \log \left[\frac{\gamma_2 + \sqrt{r_2^2 + \gamma_2^2 - \left(\frac{2+\Delta}{2} \right) r^2}}{\gamma_1 + \sqrt{r_2^2 + \gamma_1^2 - \left(\frac{2+\Delta}{2} \right) r^2}} \right] \right\}$$

$$(iii) \text{ for } \left[\frac{2}{2+\Delta}(r_2^2 + r_1^2) \right] \leq r \leq \left[\frac{2}{2+\Delta}(r_1^2 + r_2^2) \right] \quad (A8)$$

$$n_b(r) = \frac{4Nv_b}{\lambda_B r} \sqrt{\frac{1}{2} \left(\frac{2+\Delta}{2+\Delta} \right)} \times$$

$$\left\{ \frac{r_2}{2} \left[\sqrt{r_2^2 + r_2^2 - \left(\frac{2+\Delta}{2} \right) r^2} - \sqrt{r_1^2 + r_2^2 - \left(\frac{2+\Delta}{2} \right) r^2} \right] \right.$$

$$- \frac{1}{2} \left[r_1^2 - \left(\frac{2+\Delta}{2} \right) r^2 \right] \log \left[\frac{r_2 + \sqrt{r_1^2 + r_2^2 - \left(\frac{2+\Delta}{2} \right) r^2}}{\sqrt{\left(\frac{2+\Delta}{2} \right) r^2 - r_1^2}} \right]$$

$$\left. + \frac{1}{2} \left[r_2^2 - \left(\frac{2+\Delta}{2} \right) r^2 \right] \log \left[\frac{r_2 + \sqrt{r_2^2 + r_2^2 - \left(\frac{2+\Delta}{2} \right) r^2}}{\sqrt{\left(\frac{2+\Delta}{2} \right) r^2 - r_2^2}} \right] \right\}$$

$$(iv) \text{ for } \left[\frac{2}{2+\Delta}(r_1^2 + r_2^2) \right] \leq r \leq \left[\frac{2}{2+\Delta}(r_2^2 + r_2^2) \right] \quad (A9)$$

$$n_b(r) = \frac{4Nv_b}{\lambda_B r} \sqrt{\frac{1}{2} \left(\frac{2+\Delta}{2+\Delta} \right)} \times$$

$$\left\{ \frac{r_2}{2} \sqrt{r_2^2 + r_2^2 - \left(\frac{2+\Delta}{2} \right) r^2} \right.$$

$$\left. + \frac{1}{2} \left[r_2^2 - \left(\frac{2+\Delta}{2} \right) r^2 \right] \log \left[\frac{r_2 + \sqrt{r_2^2 + r_2^2 - \left(\frac{2+\Delta}{2} \right) r^2}}{\sqrt{\left(\frac{2+\Delta}{2} \right) r^2 - r_2^2}} \right] \right\}$$

REFERENCES

- ¹J. P. Vandevender, J. A. Swegle, D. J. Johnson, K. W. Bieg, E. J. T. Burns, J. W. Poukey, P. A. Miller, J. N. Olsen, and G. Yonas, *Laser and Particle Beams* 3, 93 (1985).
- ²P. L. Dreike, E. J. T. Burns, S. A. Slutz, J. T. Crow, D. J. Johnson, P. R. Johnson, R. J. Leeper, P. A. Miller, L. P. Mix, D. B. Seidel, and D. F. Wenger, *J. Appl. Phys* 60, 878, (1986).
- ³G. Yonas, *Bull. Am. Phys. Soc.* 21, 1102 (1976).
- ⁴D. A. Hammer and N. Rostoker, *Phys. Fluids* 13, 1831 (1970).
- ⁵D. Mosher and W. W. Hsing, *Bull. Am. Phys. Soc.* 22, 1198 (1977).
- ⁶P. F. Ottinger, D. Mosher, and Shyke A. Goldstein, *Phys. Fluids* 23, 909 (1980).
- ⁷D. Mosher, G. Cooperstein, Shyke A. Goldstein, D. G. Colombant, P. F. Ottinger, F. L. Sandel, S. J. Stephanakis, and F. C. Young, in The Proceedings of the Third International Topical Conference on High Power Electron and Ion Beam Research and Technology (Novosibirsk, USSR, 1979), p. 576.

⁸P. F. Ottinger, Shyke A. Goldstein, and D. Mosher,
NRL Memorandum Report 4948, Nov. 12, 1982.

⁹P. F. Ottinger, S. A. Goldstein, and D. Mosher, in Conference
Record of the 1980 IEEE International Conference on Plasma Science,
(Madison, WI, 1980), p. 98

¹⁰J. Watrous, P. F. Ottinger, and D. Mosher, NRL Memorandum Report
(in preparation)

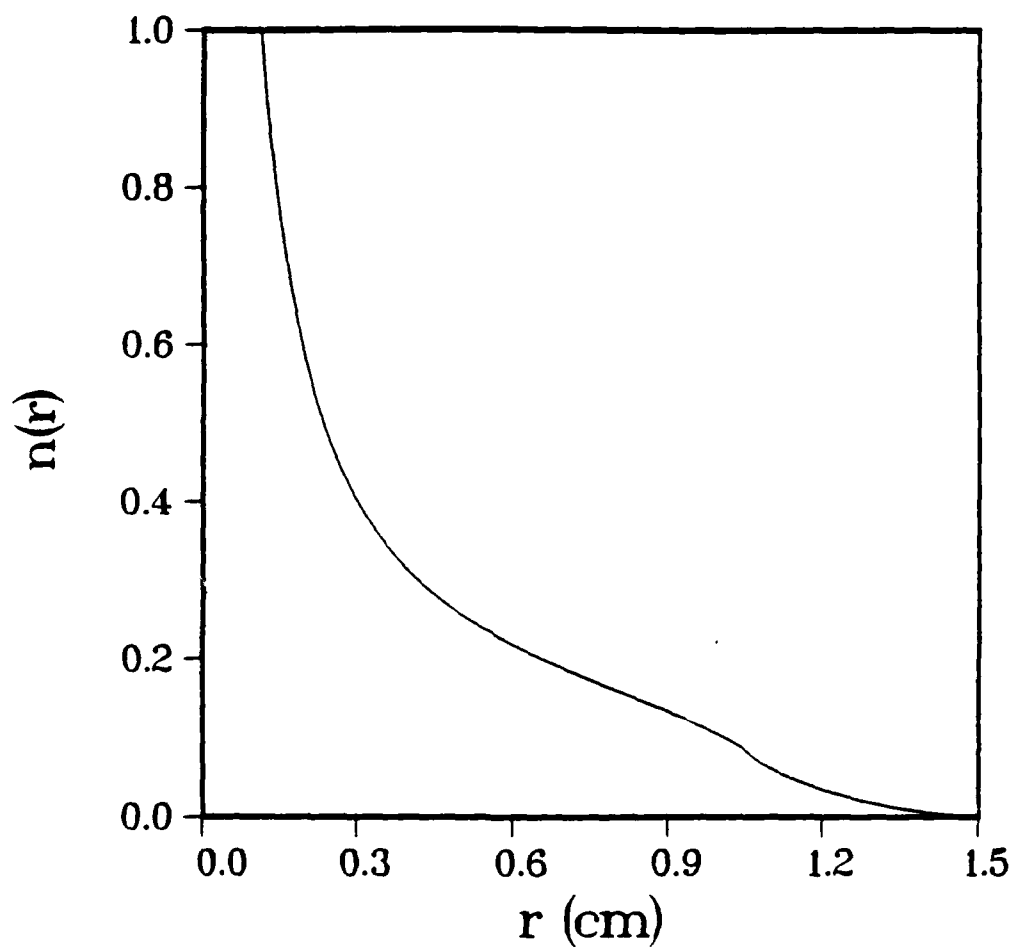


Figure 1: A typical focused ion beam number density profile exhibiting the characteristic $1/r$ shape. The initial distribution filled a rectangular region in the radial phase space plane defined by $0 < r < 2.12$ cm and $0 < |v_r/v_b| < 0.0598$.

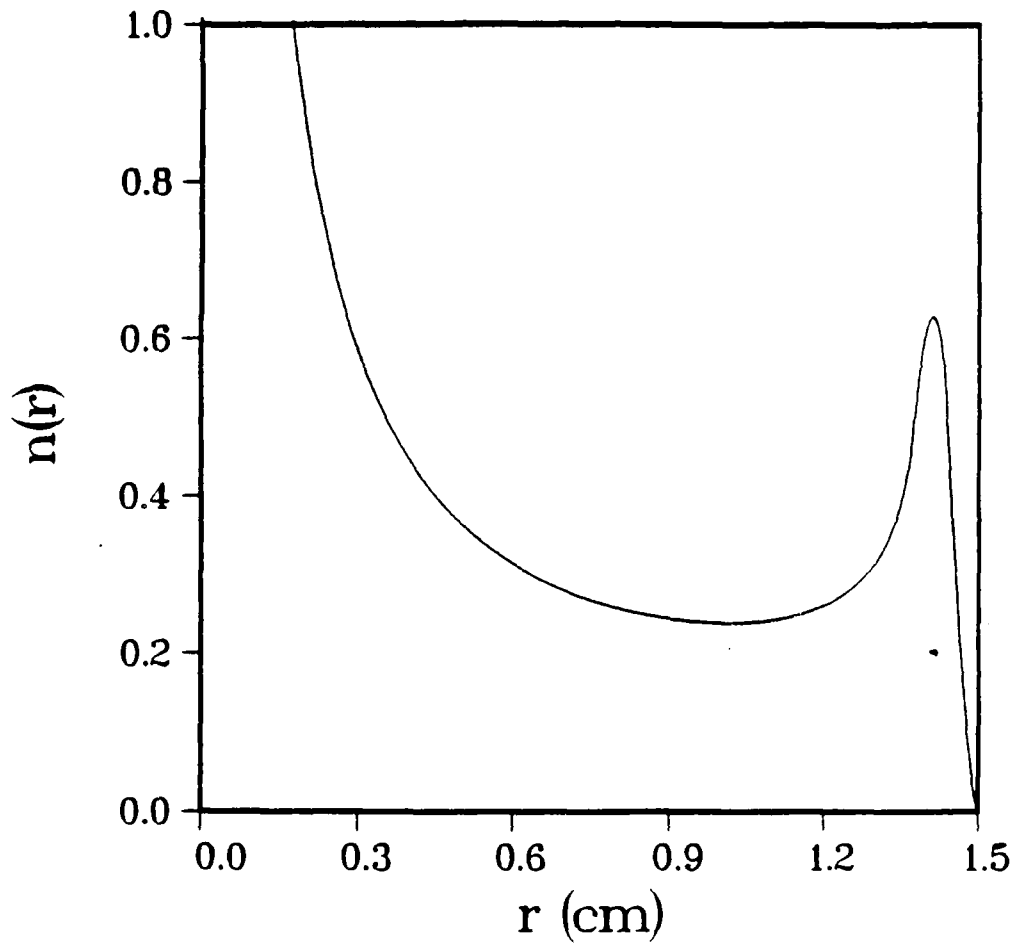


Figure 2: A focused ion beam number density profile exhibiting a strong off-axis peak in addition to the characteristic $1/r$ shape. In this example, the initial distribution filled a rectangle defined by $1.94 \text{ cm} < r < 2.12 \text{ cm}$ and $0.0548 < |v_r/v_b| < 0.0598$.

WALL STABILIZED, LIGHT-ION BEAM TRANSPORT AND FINAL FOCUSING SYSTEM

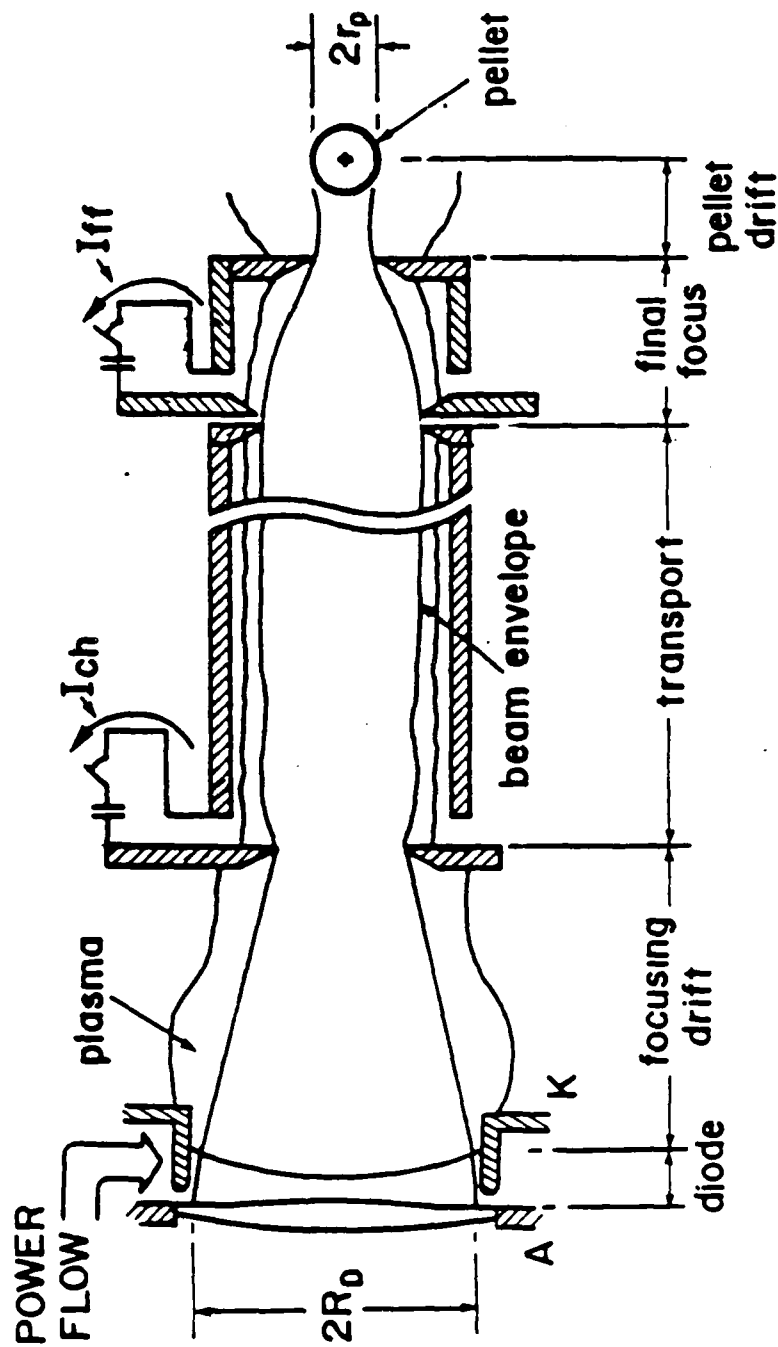


Figure 3: The main components of the ion beam production and focusing system.

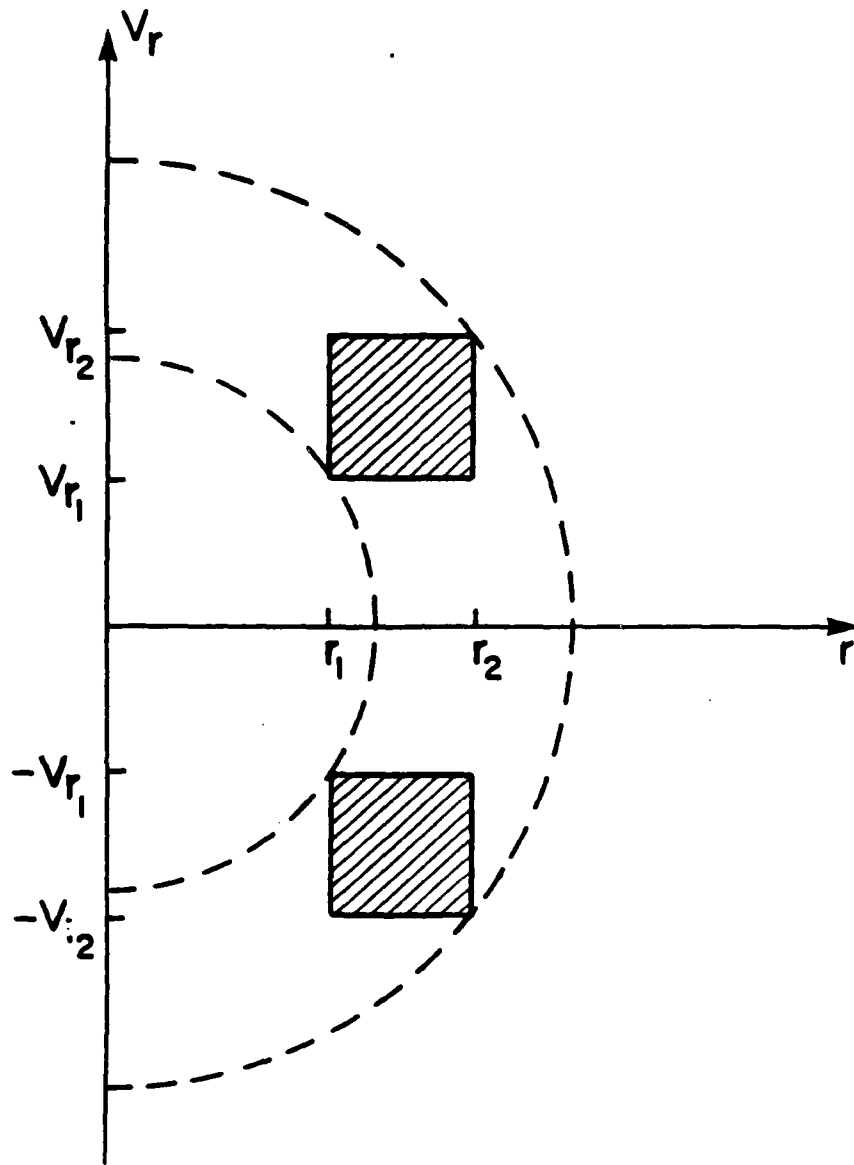


Figure 4: The phase mixed distribution compared to the initial distribution.

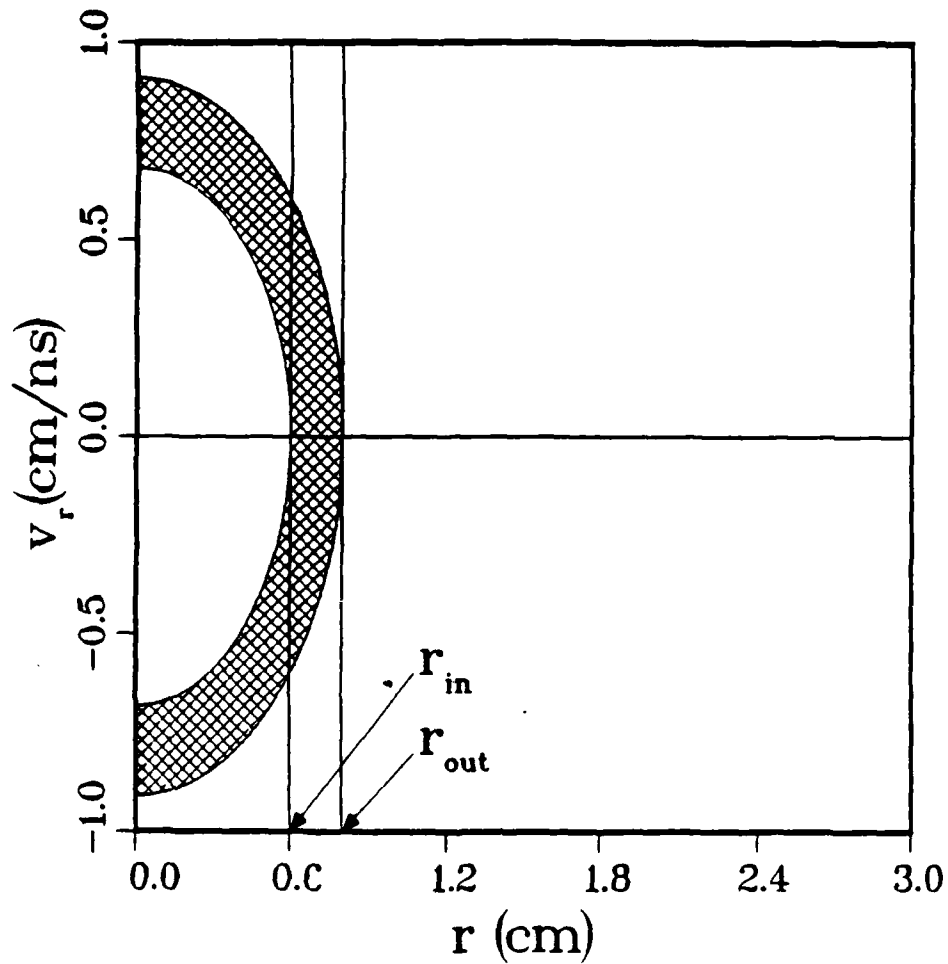


Figure 5: Illustration of the requirement placed on the phase mixed and focused ion beam radial phase space distribution for developing the source brightness requirements. The intersection of the ellipse that defines the ion beam phase space distribution with the v_r axis must coincide with the target annulus $r_{in} \leq r \leq r_{out}$.

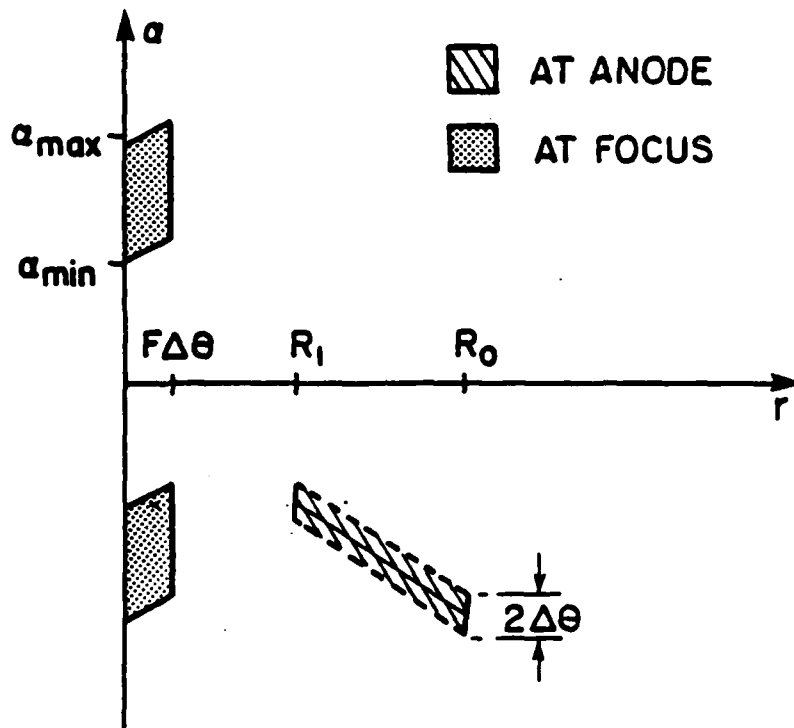


Figure 6: Phase space diagram for pinched focusing.

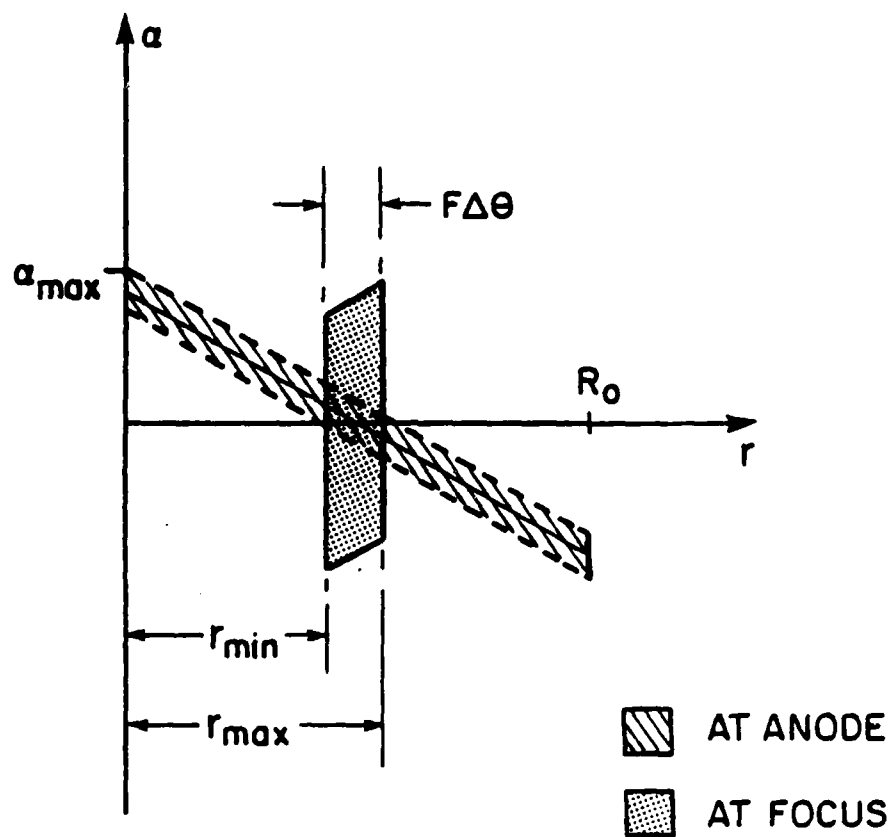


Figure 7: Phase space diagram for annular focusing.

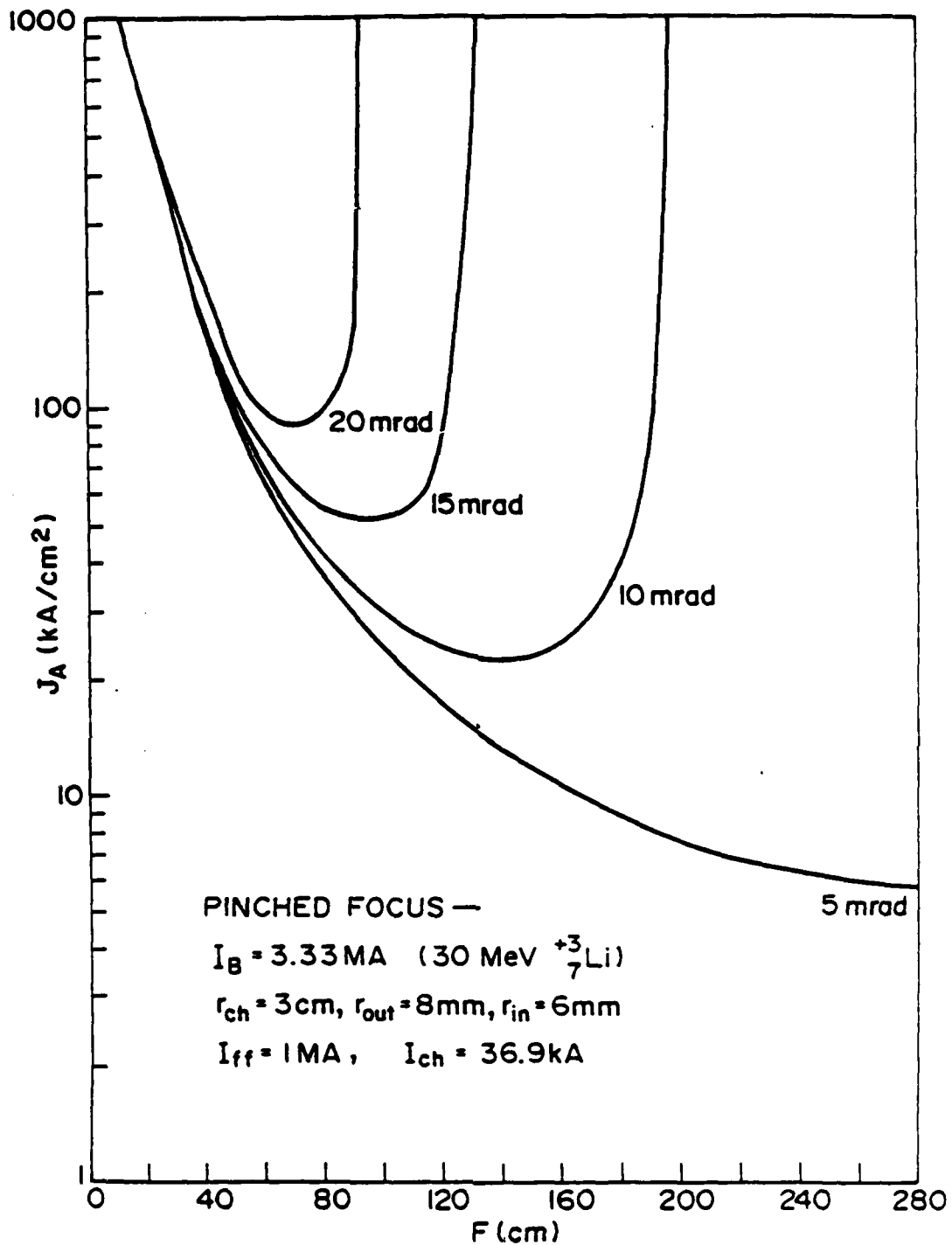


Figure 8: The anode current density for pinched focusing as a function of the focal length and the microdivergence.

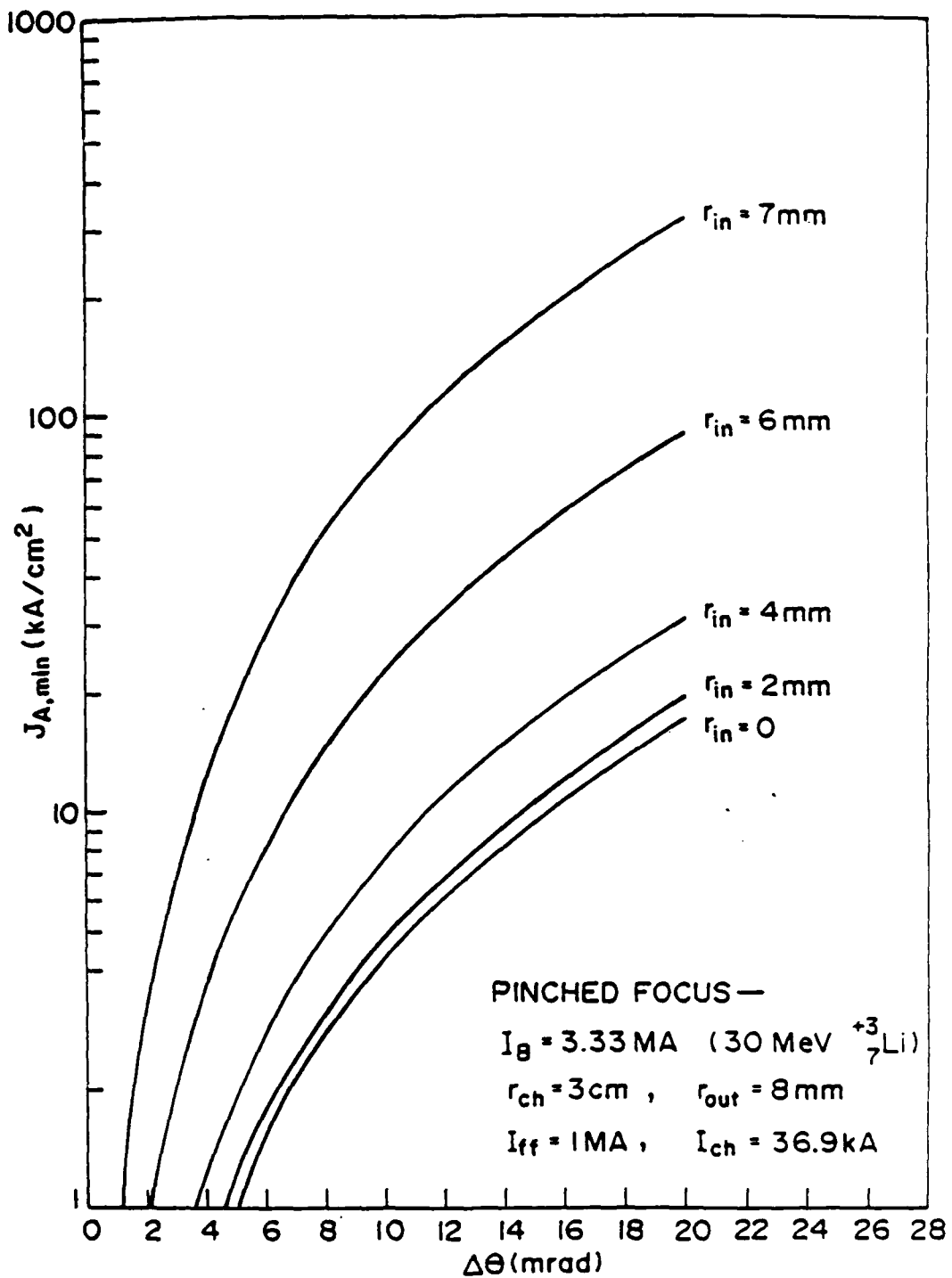


Figure 9: The minimum anode current density for pinched focusing - high current case.

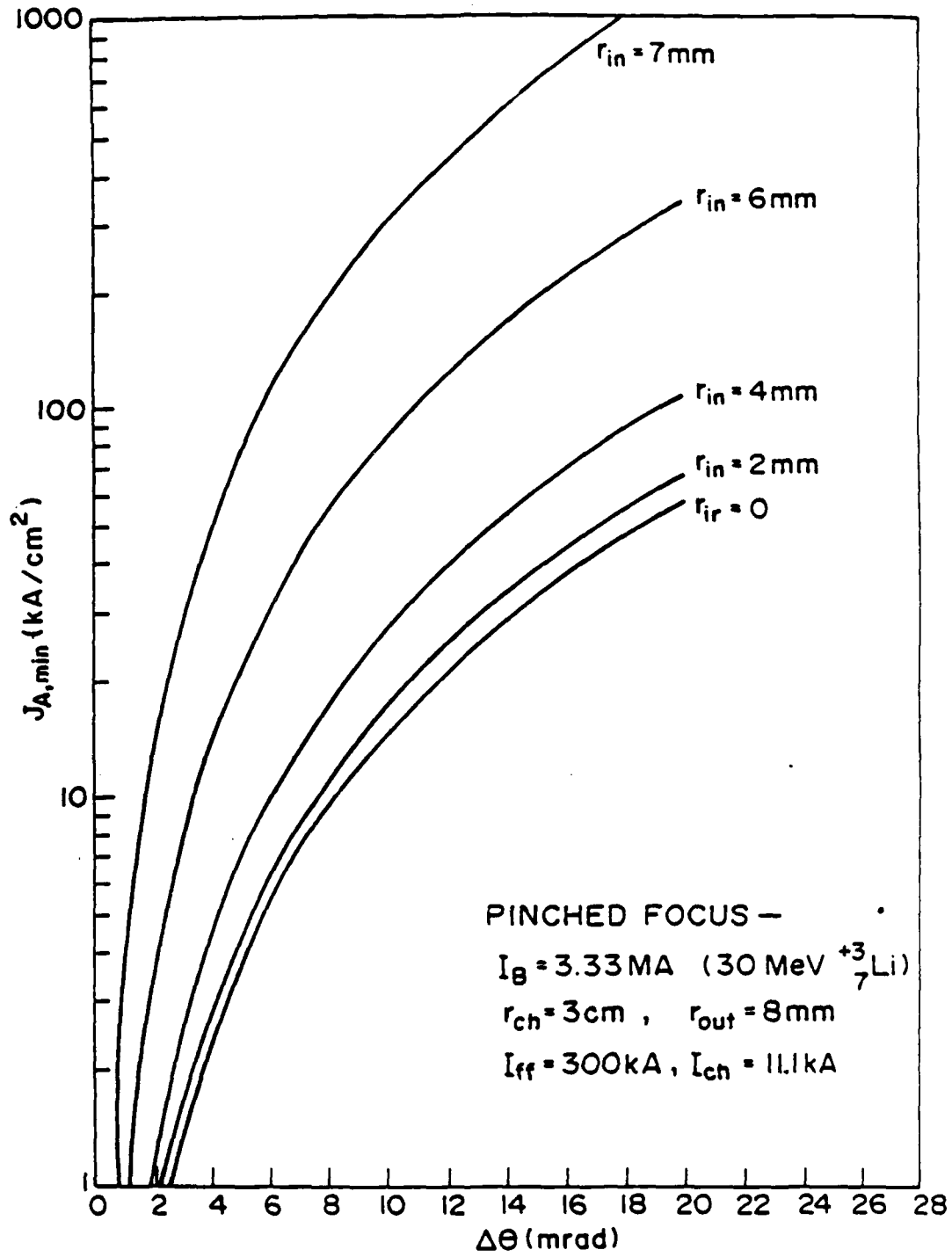


Figure 10: The minimum anode current density for pinched focusing - low current case.

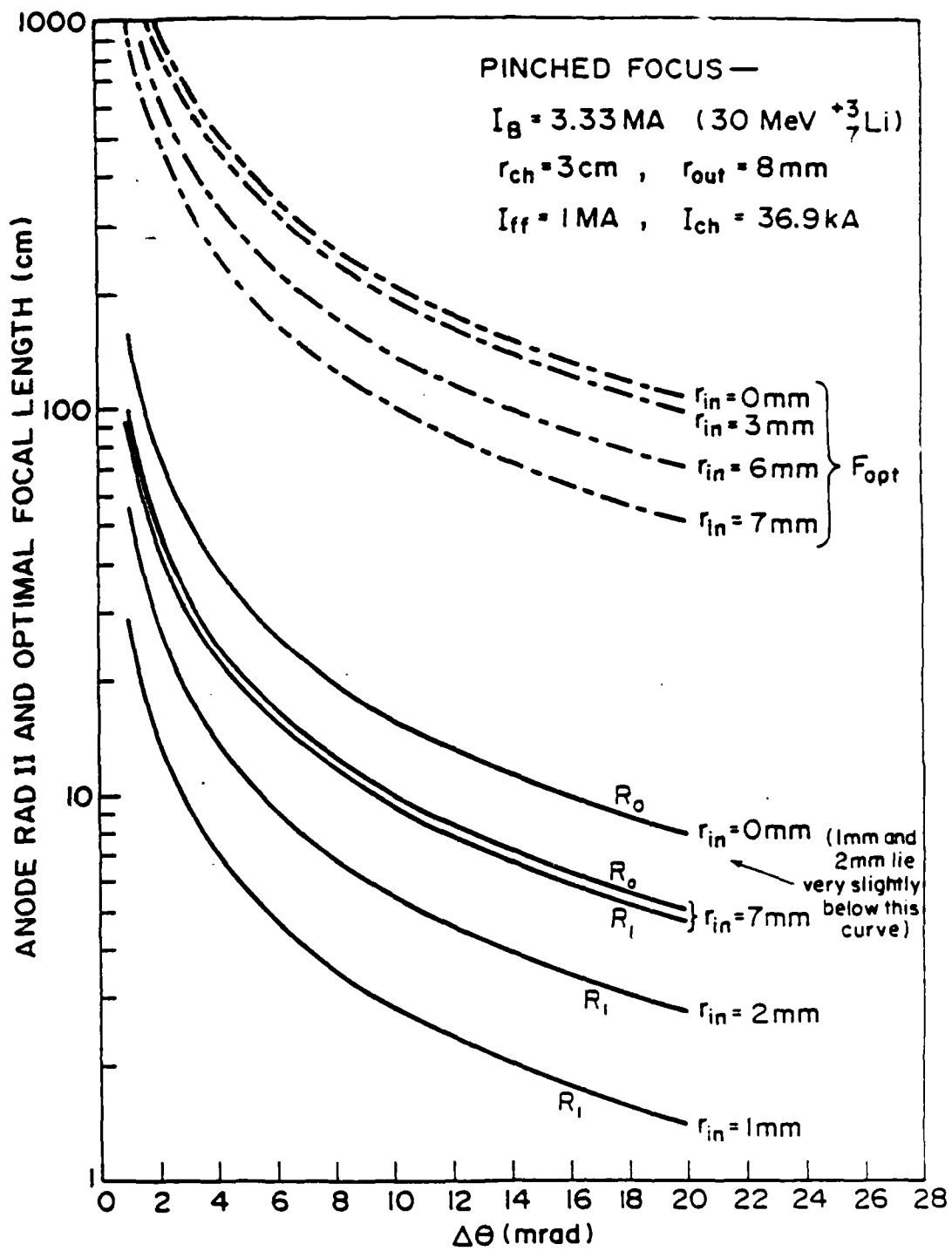


Figure 11: Inner and outer anode radii and optimal focal length as functions of the microdivergence - low current case.

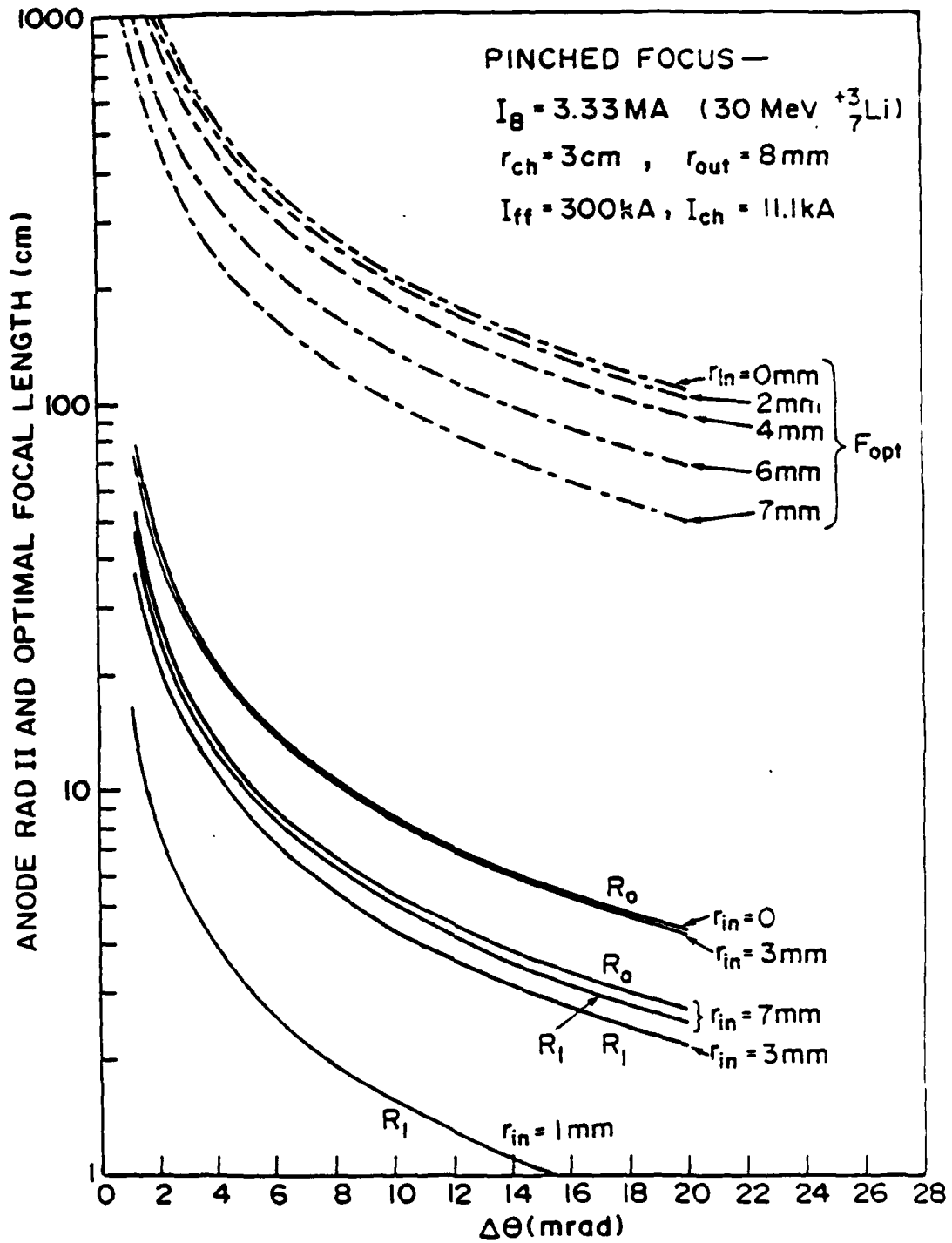


Figure 12: Inner and outer anode radii and optimal focal length as functions of the microdivergence - high current case.

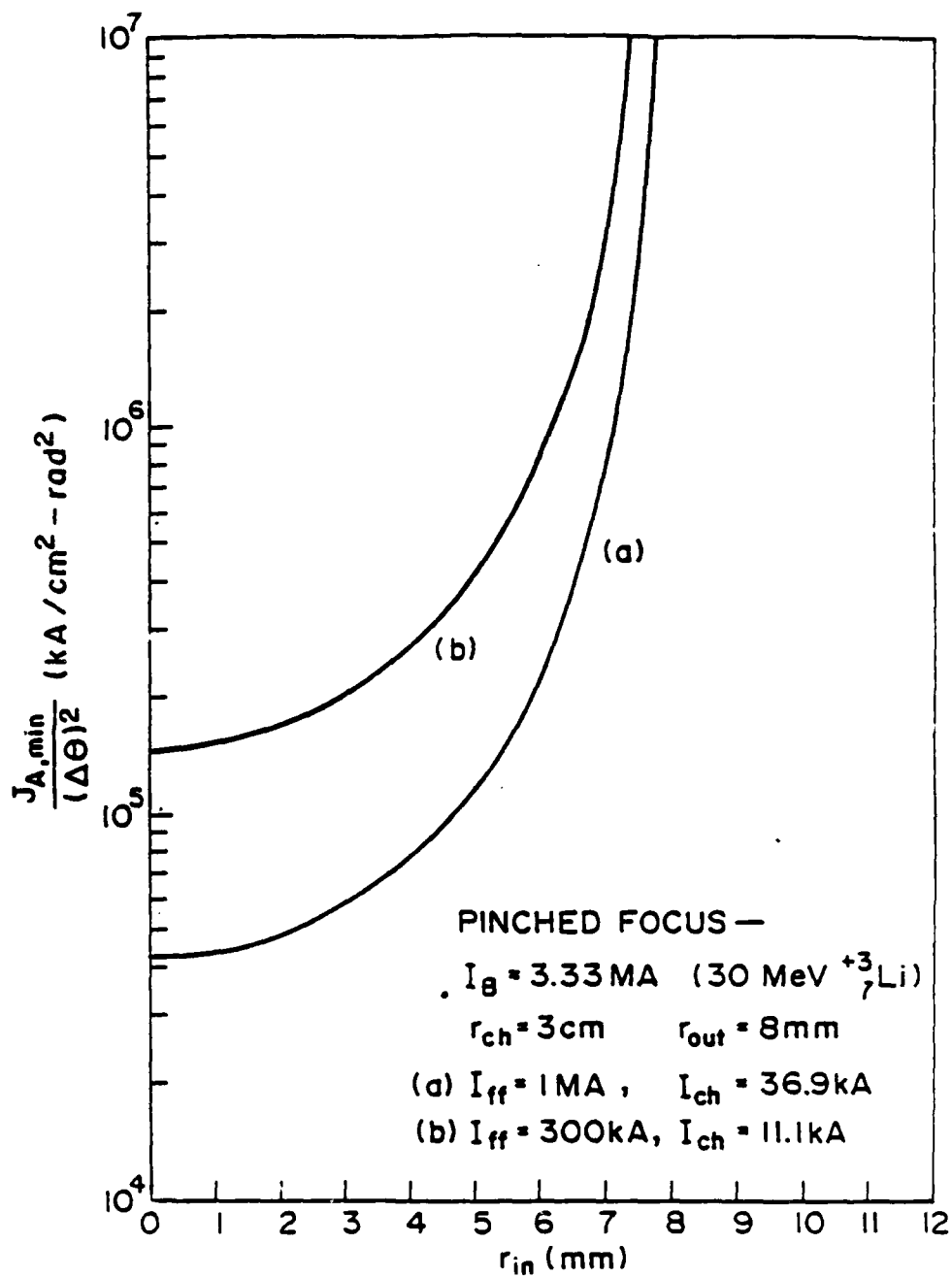


Figure 13: Source brightness as a function of the inner radius of the target annulus for pinched focusing.

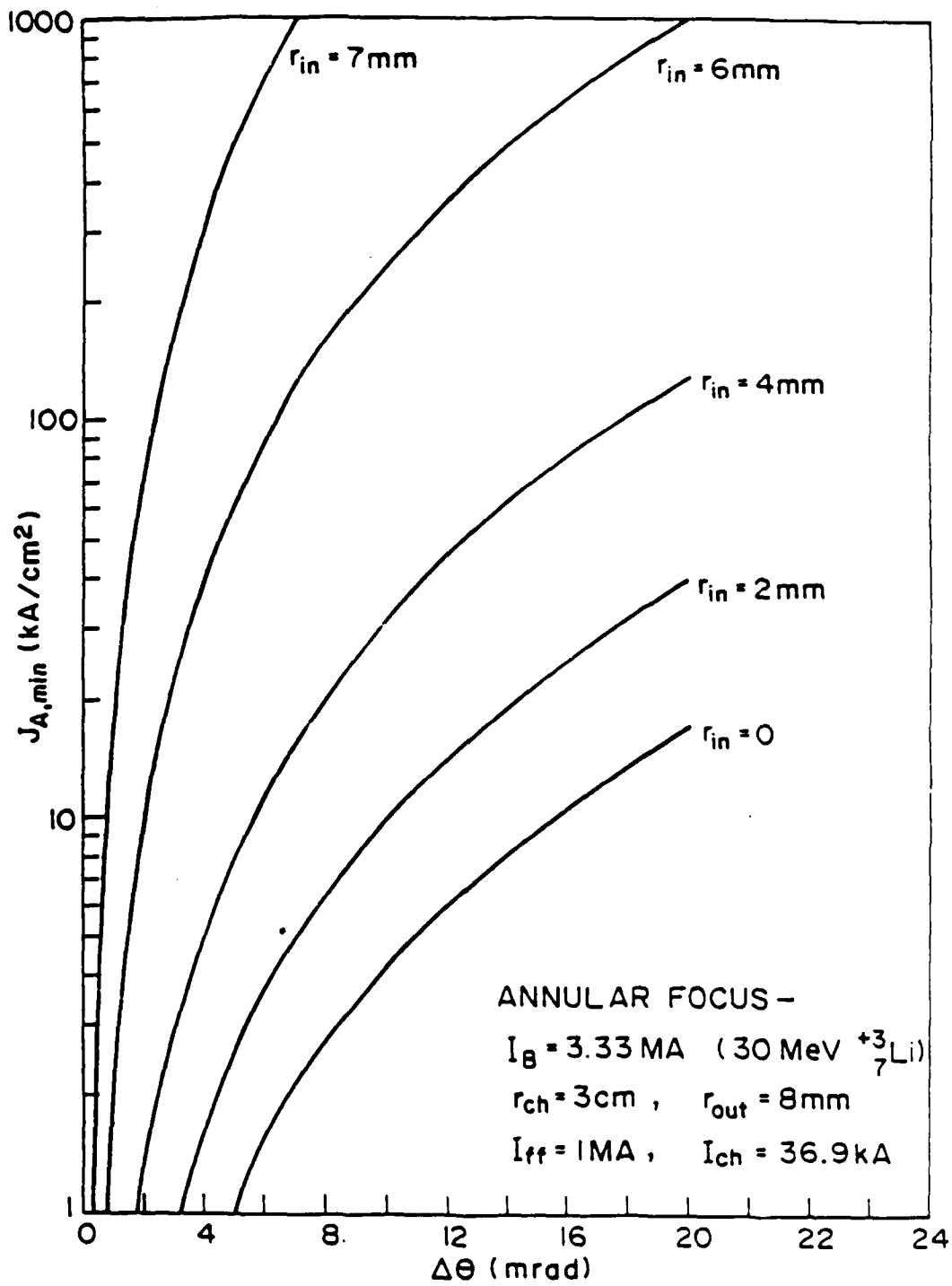


Figure 14: The minimum anode current density for annular focusing - high current case.

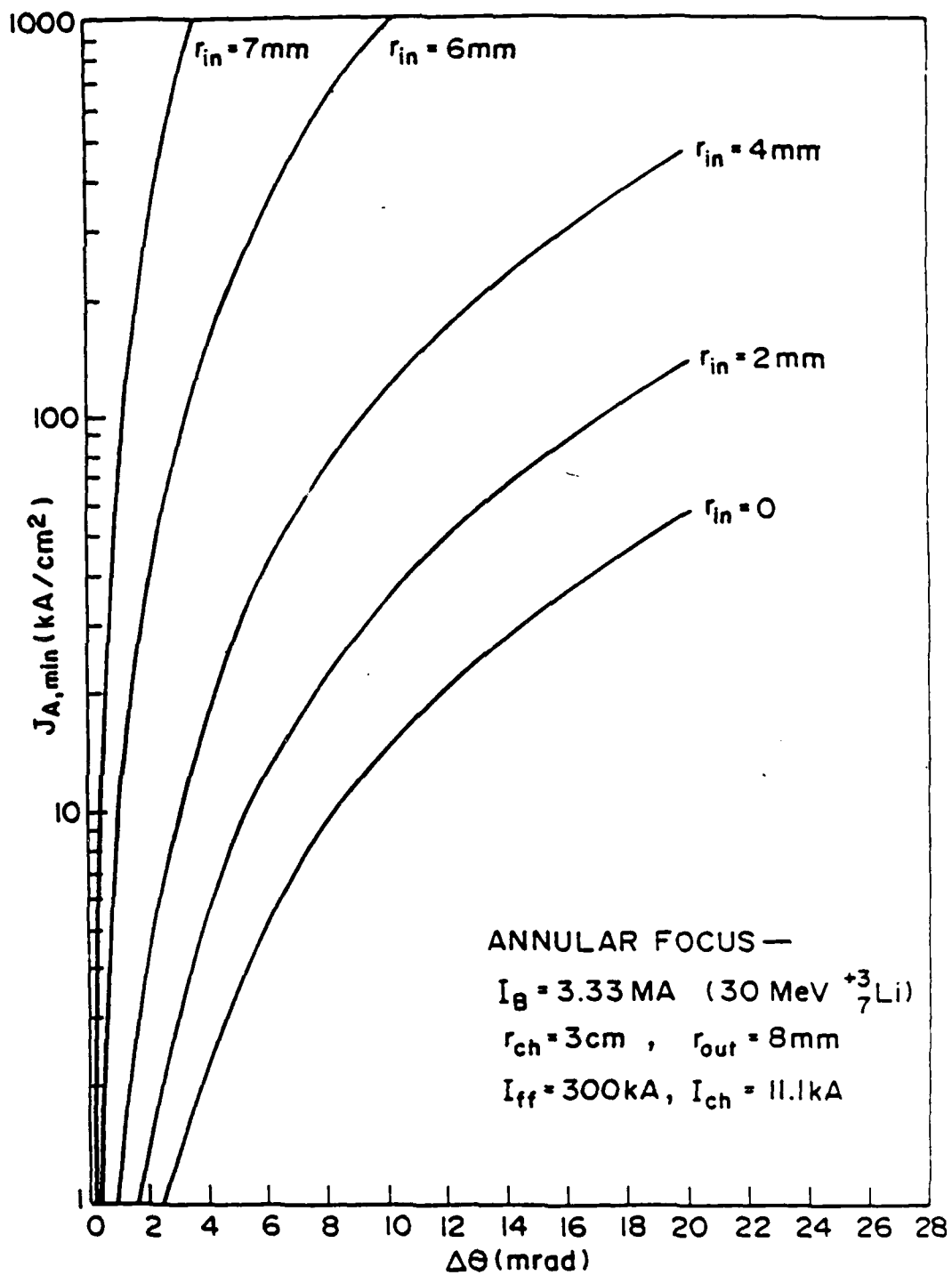


Figure 15: The minimum anode current density for annular focusing - low current case.

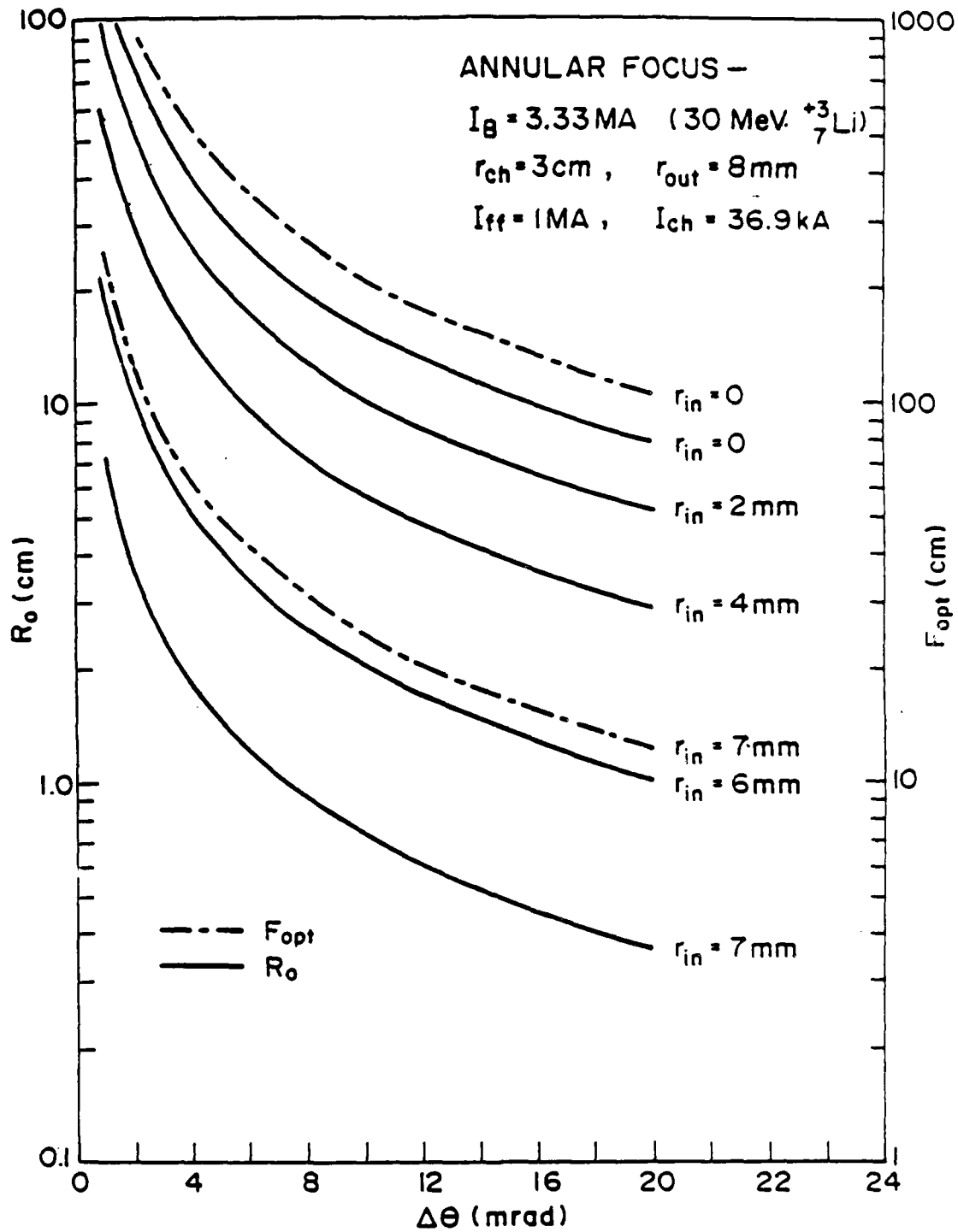


Figure 16: Inner and outer anode radii and optimal focal length as functions of the microdivergence - low current case.

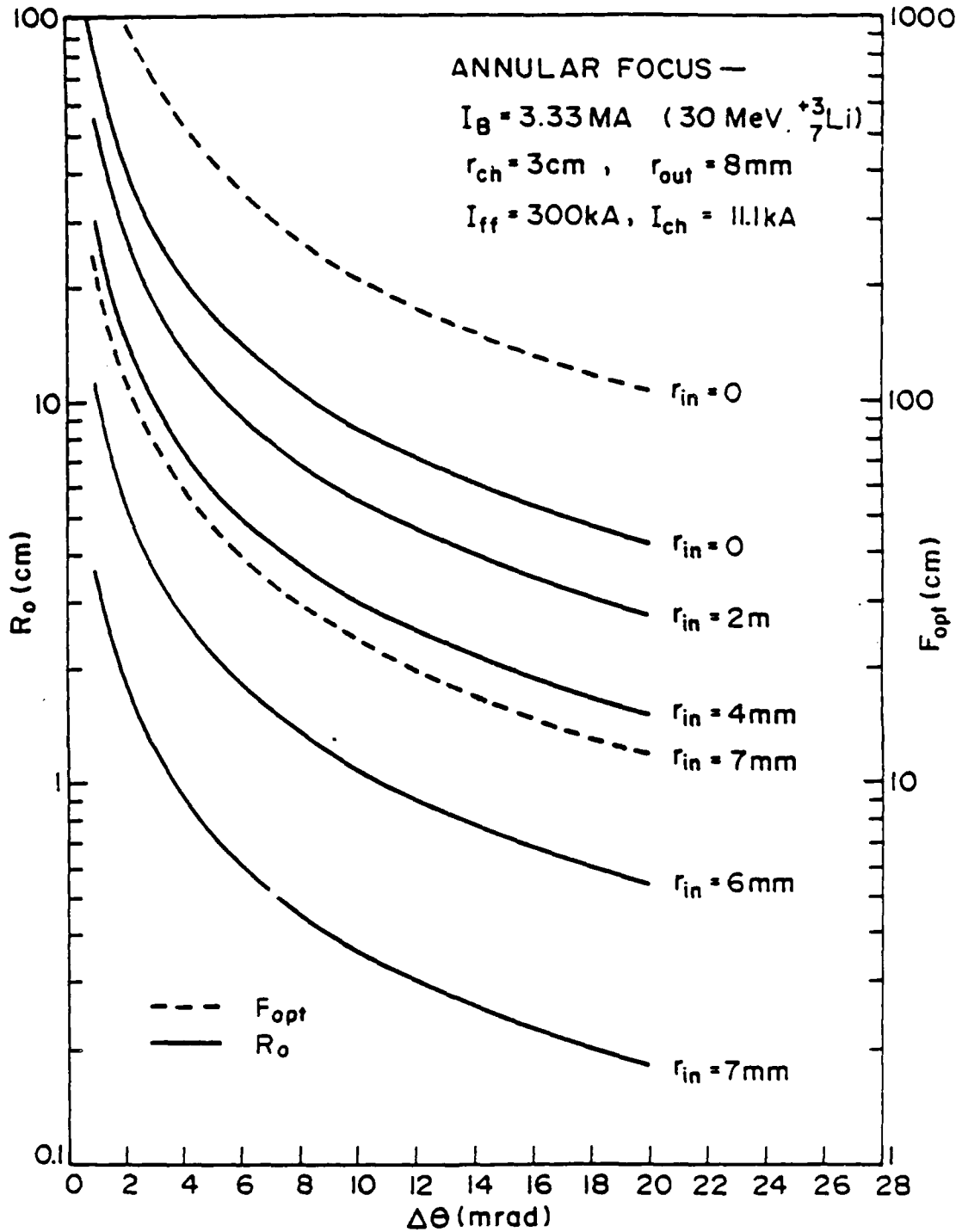


Figure 17: Inner and outer anode radii and optimal focal length as functions of the microdivergence - high current case.

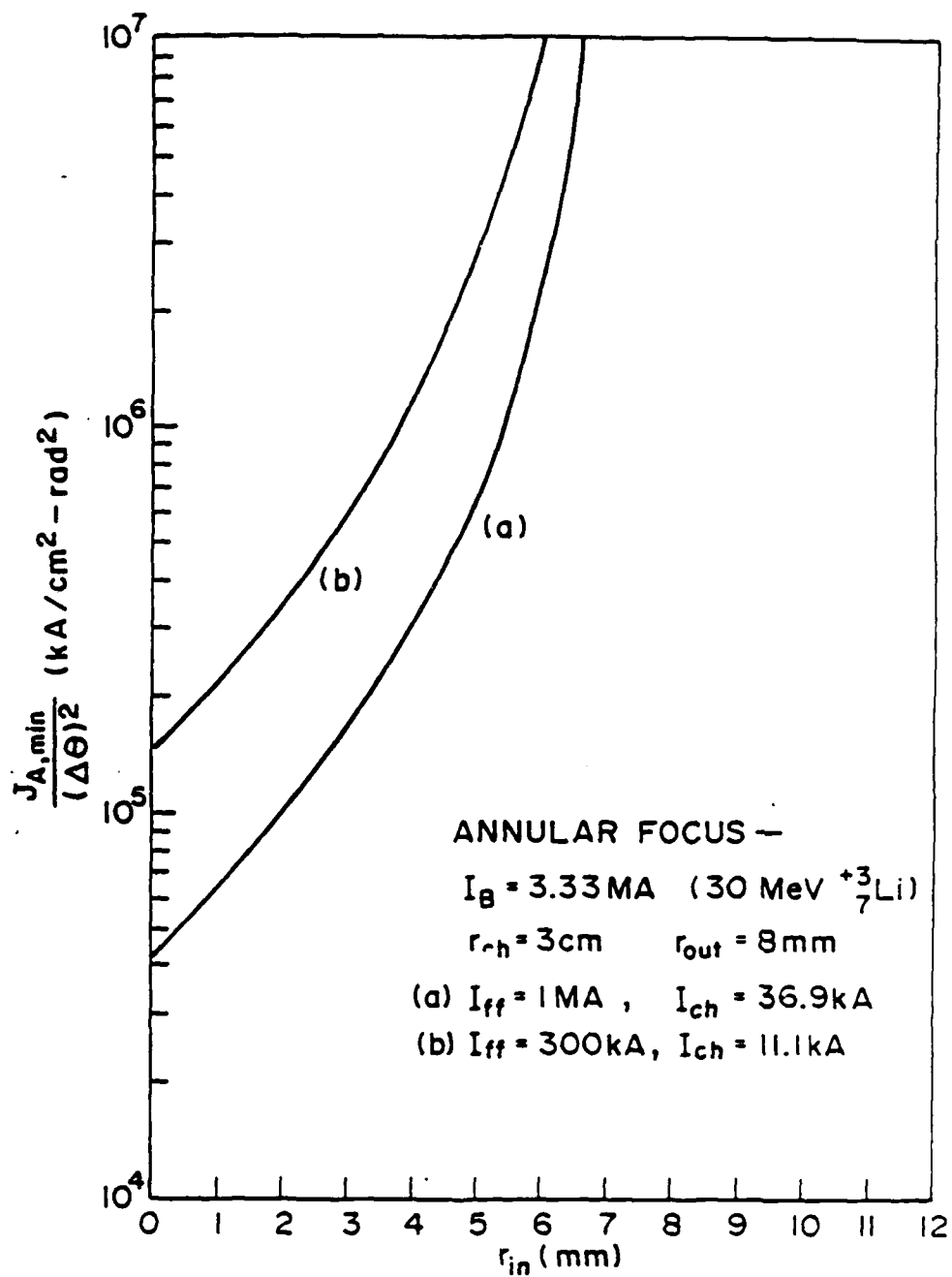


Figure 18: Source brightness as a function of the inner radius of the target annulus for annular focusing.

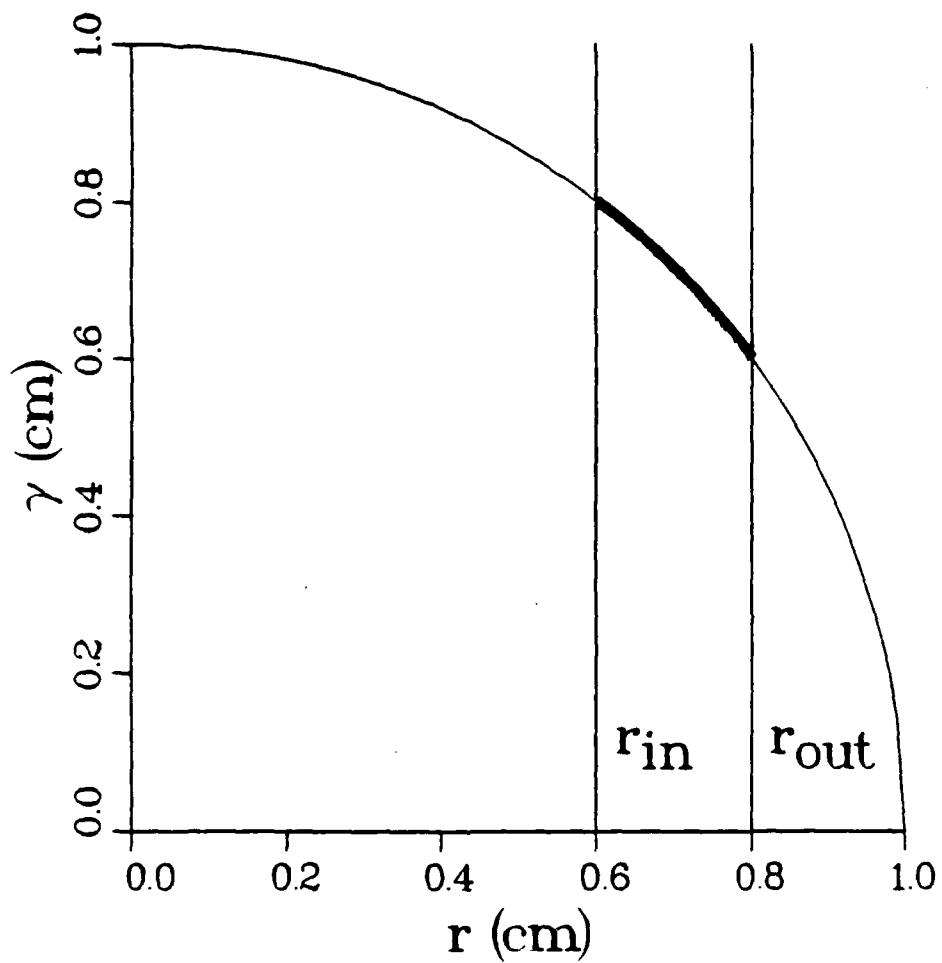


Figure 19: Illustration of the calculation of the zero emittance limit of the delivery efficiency. The focused beam radius is 1 cm. The efficiency is the ratio of the arc-length of the darkened portion of the quarter circle to the arc-length of the entire quarter circle.

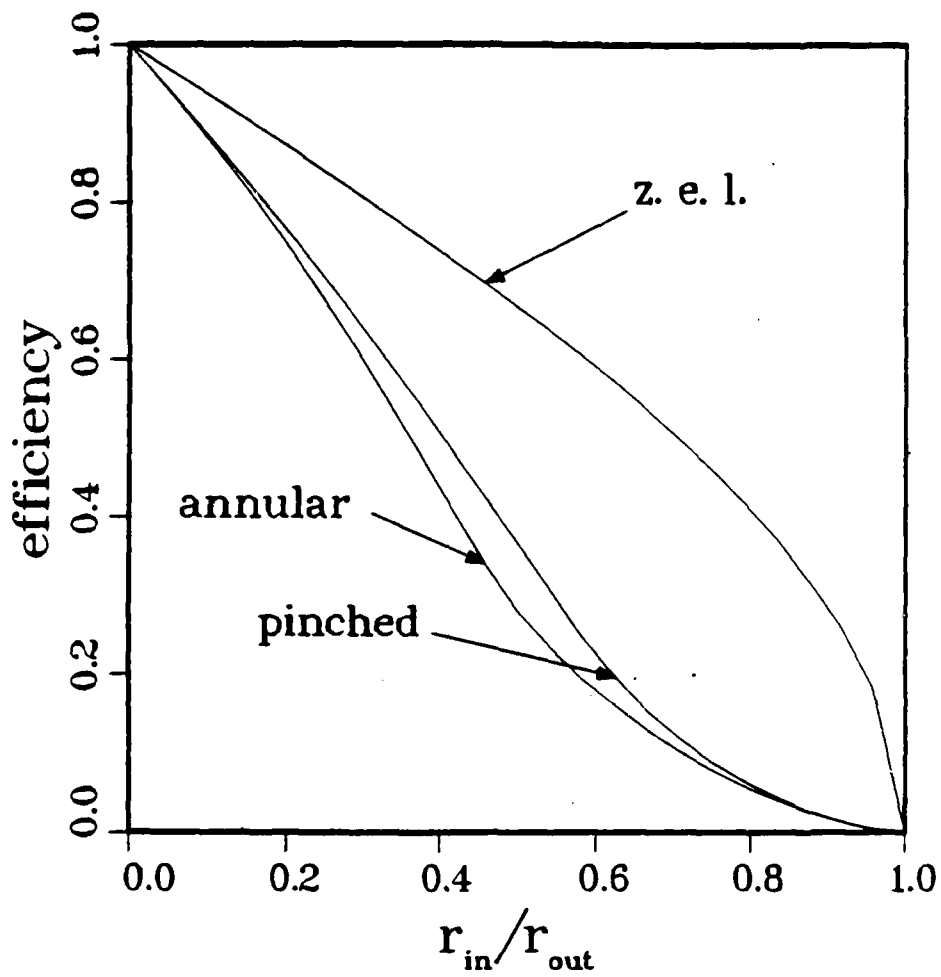


Figure 20: The delivery efficiency as a function of r_{in} for pinched focusing. Also plotted is the delivery efficiency in the zero emittance limit.

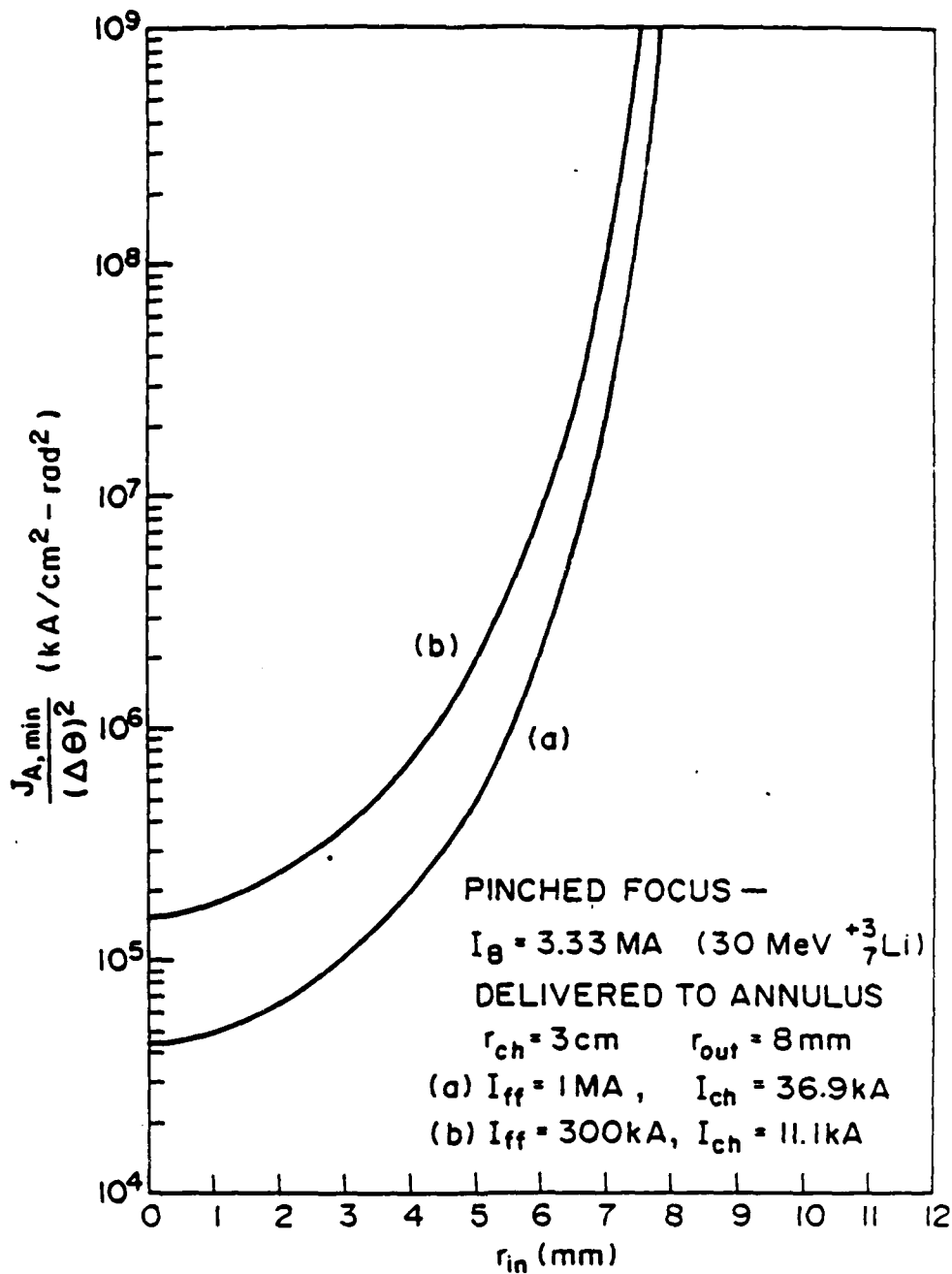


Figure 21: The delivery efficiency as a function of r_{in} for annular focusing. Also plotted is the delivery efficiency in the zero emittance limit.

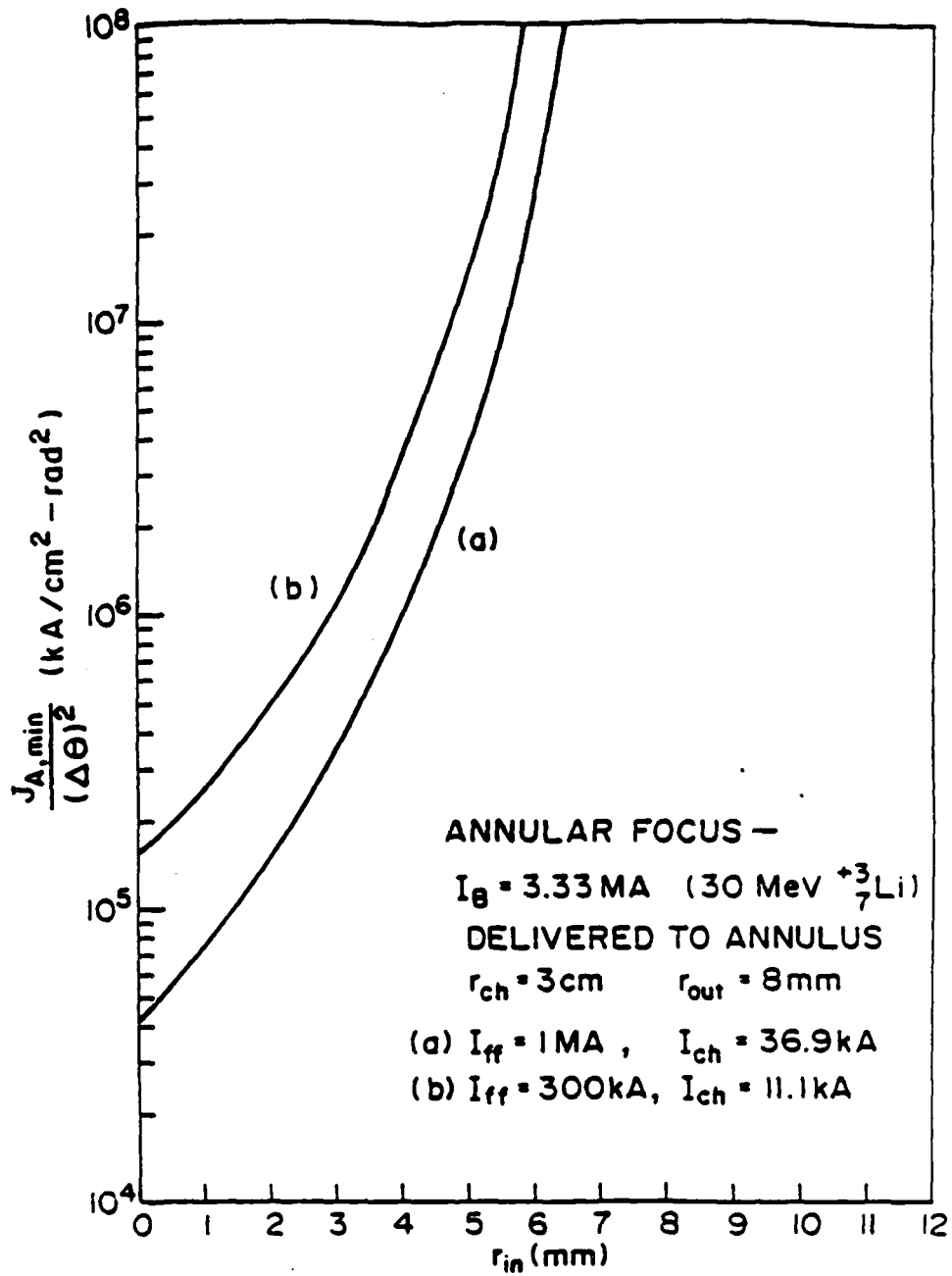


Figure 22: The source brightness required to deliver the required ion beam current to the target annulus for pinched focusing.

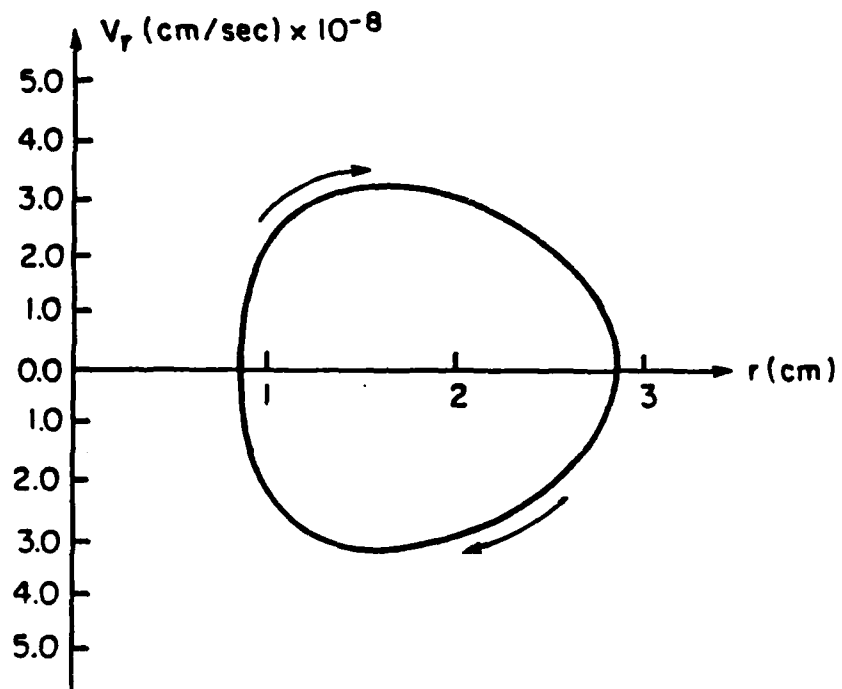


Figure 23: The source brightness required to deliver the required ion beam current to the target annulus for annular focusing.

DISTRIBUTION FOR DOE SPONSORED WORK
15 March 1988

U.S. Department of Energy Office of Inertial Fusion Washington, DC 20545 Attn: S.L. Kahalas 1 copy R.L. Schriever 1 copy	Lawrence Livermore National Laboratory P.O. Box 808 Livermore, CA 94550 Attn: R. Bazel/J. Kahn, L-1 1 copy J. Emmett, L-488 1 copy W. Krupke, L-488 1 copy E. Storm, L-481 1 copy J. Lindl, L-477 1 copy
U.S. Department of Energy Office of Classification Washington, DC 20545 Attn: Robert T. Duff 1 copy	Los Alamos Scientific Laboratory P.O. Box 1663 Los Alamos, NM 87545 Attn: S.D. Rockwood, ICF Prog. Mgr. DAD/IF/M/S 527 1 copy
U.S. Department of Energy Nevada Operations Office P.O. Box 14100 Las Vegas, NV 89114 2 copies	Naval Research Laboratory 4555 Overlook Ave., S.W. Washington, D.C. 20375-5000 Attn: Code/Name
U.S. Department of Energy P.O. Box 62 Oak Ridge, TN 37830 1 copy	2628/TID Dist 22 copies 1000/T. Coffey 1 copy 4000/W. Ellis 1 copy 4040/J. Boris 1 copy 4700/S.L. Ossakow 26 copies 4701/I. Vitkovitsky 1 copy 4710/C. Kapetanakis 1 copy 4720/J. Davis 1 copy 4730/S. Bodner 1 copy 4740/W. Manheimer 1 copy 4750/R. Meger 1 copy 4760/B. Robson 1 copy 4770/G. Cooperstein 10 copies 4770.1/F. Young 1 copy 4770.1/D. Mosher 1 copy 4770.2/R. Commisso 1 copy 4771/P. Ottinger 1 copy 4771/J. Neri 1 copy 4771/J. Grossmann 1 copy 4773/S. Stephanakis 1 copy 4790/D. Colombant 1 copy 4790/I. Haber 1 copy 4790/M. Lampe 1 copy 4600/D. Nagel 1 copy
Cornell University Ithaca, NY 14850 Attn: D.A. Hammer 1 copy R.N. Sudan 1 copy	
Defense Technical Information Center Station Duke Street Alexandria, VA 22314 Attn: T.C. 2 copies	
JAYCOR, Inc. 1608 Spring Hill Rd. Vienna, VA 22180-2270 Attn: B.V. Weber 1 copy D.D. Hinshelwood 1 copy	
KMS Fusion, Inc. 3941 Research Park Drive P.O. Box 1567 Ann Arbor, MI 48106 Attn: A.A. Glass 1 copy	
Lawrence Berkley Laboratory Berkley, CA 94720 Attn: D. Keefe 1 copy	
Director of Research U.S. Naval Academy Annapolis, MD 21402 2 copies	Sandia National Laboratories P.O. Box 5800 Albuquerque, NM 87185 Attn: J.P. VanDevender/1200 1 copy D.L. Cook/1250 5 copies T. Martin/1250 1 copy
Records 1 copy	University of Rochester 250 East River Road Rochester, NY 14623 Attn: J. Eastman 1 copy
Code 1220 1 copy	
Code 2634 Cindy Sims 1 copy	